

Chapter 3

Drift Velocity Monitor for the ALICE TPC

3.1 Introduction

Gaseous detectors (multi-wire proportional chambers, drift chambers and TPCs) among others are nowadays frequently used in many experiments around the world. They provide information about particle tracks being created during collisions between projectile and target particles. The active volume of currently constructed gas detectors reaches values in the order of 10^2 m^3 (for instance the ALICE¹ TPC [TPC01] will have an active volume of 88 m^3). Such a large volume requires a special attention to ensure isotropic conditions as a whole active volume of the detector as well as to provide stable conditions during detector operating. To obtain such conditions a number of controlling systems must be used. Since the gas detectors are very sensitive to the ambient conditions as temperature and pressure, specially those using CO_2 in the gas mixture, they require the online monitoring of the gas properties (gain, drift velocity, composition, etc.). One of the frequently used gas monitoring system is known as GOOFIE [Lip00]. The GOOFIE is traditionally used to monitor the drift velocity in drift chambers (or TPCs). We extend its use to monitor also the gain (in order to determine the ternary gas composition).

The ALICE experiment is located at the **L**arge **H**adron **C**ollider (LHC) [Pot96] optimized for the study of heavy-ion collisions, at a center-of-mass energy of 5.5 TeV per nucleon pair. Such collision energy allows one to study properties of strongly interacting matter into a radically new energy region, previously reached only in the interactions of the highest energy cosmic rays. All parameters relevant to the formation of the QGP, as the energy density, the size and the lifetime of the system, will be increased by large factors, more than an order of

¹A Large Ion Collider Experiment

magnitude in comparison with previous accelerator experiments. The initial temperatures will largely exceed the calculated critical temperature for QGP formation which allow one to study, in detail, nonperturbative aspects of QCD such as the deconfinement and the chiral symmetry restoration. Moreover, it will be possible to exploit a wider set of relevant observables (see Section 1.2.4) as compared to previous experiments, thus substantially enhancing the understanding of the properties of the quark-gluon plasma. The hard probes, which are sensitive to the nature of the medium at the earliest stages of the collision, will be explored at higher energy and higher luminosities. In addition, the expected very high multiplicity, several thousands of charged particles per pseudorapidity unit, will allow to measure a large number of observables on an event-by-event basis as the impact parameter, the multiplicity, the particle composition and the spectra, as well as the correlation function between different particles species. Therefore single event analysis, and in particular the study of non-statistical fluctuations associated to the critical phenomena, can be effectively performed at the LHC.

The choice of the gas mixture of the TPC depends on the specific requirements of the experimental setup as it was already mentioned in Section 2.4.1. Therefore, after detailed research [Gar04, Vee03] the Ne-CO₂-N₂ [90-10-5] gas mixture was chosen for the ALICE TPC. The expected high multiplicity ($dN/dy = 8000$ at the time of the design) and the required momentum resolution ($dp/p=1\%$ at the multiple scattering limit) ruled out the use of argon as a noble gas because of its low ions mobility in comparison with Ne⁺. The CO₂ was the only gas that fulfilled all requirements and restrictions assumed for the quencher in ALICE TPC. Any quencher based on the hydrocarbon was unacceptable due to the high doses expected at the anode wire for the lifetime of the experiment (11 mC/cm), the modern safety regulations and the production of thermal neutrons. Performed ageing test with the P10 gas mixture on a full size prototype readout chamber has shown dramatic gain degradation equivalent to 1-2 years of ALICE operation. The small amount of nitrogen was added to the gas mixture to minimize the risk of breakdown in the form of self-sustained glow discharges. The absorption cross-section of N₂ explains the substantial quenching improvement in the neon-based mixture. Fig. 3.1 presents the photon absorption cross-section of both CO₂ and N₂ as a function of the photon energy. The main excited state of neon (16.8 eV) can be de-excited by the ionization mechanism based on the process $A + B^* \rightarrow A^+ + B + e^-$ (Penning effect). The rather low absorption cross-section of CO₂ at this energy is not able to quench all excited atoms resulting in delocalised new avalanches or induced field emissions from the cathode surface. Therefore, N₂ as an additional component of the gas mixture reduces sufficiently such effect and moreover, the drift velocity does not nearly change. Ideally, the gas composition should be preserved during the time operation of the detector. However, this is not always the case in the real experiment. Due to some imperfections in the chambers or/and the field cage the air can enter into the active volume of the detector. The well known main components of the air, N₂ and O₂ (approx. 78 % and 21 %), will slowly accumulate in the gas mixture. The purification system based on activated copper can easily remove the oxygen molecules from the active volume of the detector, however, it will not affect the nitrogen. Moreover, the CO₂ filling the containment vessels can

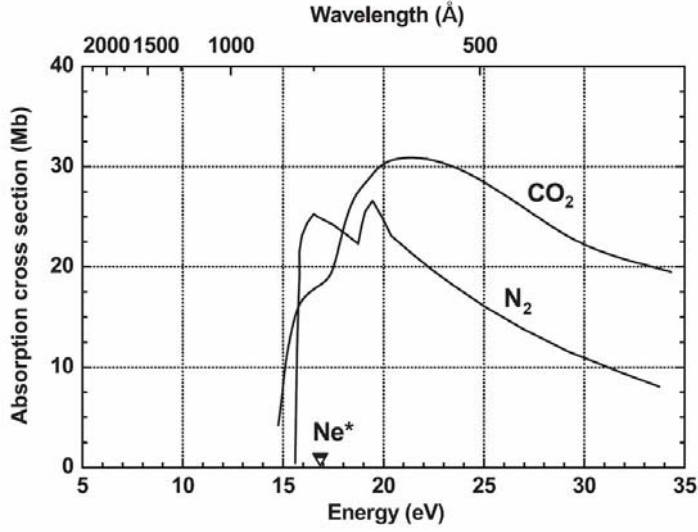


Figure 3.1: Absorption cross-section of CO_2 and N_2 as a function of the photon energy [Gar04].

mix with the TPC gas composition too. Therefore, the monitoring of the gas composition as well as the gas properties will be an integral part of the ALICE TPC slow control system. This task will be entrusted to the GOOFIE which will monitor the drift velocity together with the gas gain and from them the gas composition will be derived (see Section 3.3).

In the presence of an electric field \vec{E} , the electrons and ions freed by radiation move along the field lines towards anode and cathode respectively. This acceleration is interrupted by collisions with the gas molecules that limit the maximum average velocity. The latter can be attained by the charge along the field direction. Attained average velocity is known as the drift velocity of the charge and is superimposed upon its normal random movement. The drift speed of the ions is slow, compared to their thermal velocities, while, for electrons it can be much higher since they are much lighter. Eq. 2.8, for the case when the electric field vector \vec{E} is along the drift vector \vec{v}_d , is simplified to the form

$$\vec{v}_d = \frac{e}{m} \tau \vec{E} \quad (3.1)$$

where $(e/m)\tau$ defines the scalar mobility μ of electron-ion pairs. For a given gas mixture the drift velocity is a function of the electric field, the temperature and the pressure. For ideal gases, in which the moving charges remain in thermal equilibrium, the mobility can be shown to be related to the diffusion constant by $D/\mu = kT/e$ [PS75]. This is the result of a classical reasoning and it is known as the Einstein relation.

3.2 Experimental Setup

The goal of this research was to develop a gas monitor which will be able to determine a drift velocity for the ALICE TPC with a relative resolution in the order of 10^{-4} . The first attempts concentrated on the development of a drift velocity monitor were performed at GSI ². Further development was performed at the Max-Planck-Institut für Physik in München for the STAR FTPC³ [Mor01]. Based on the STAR FTPC gas monitor, development studies were made to achieve the required resolution and to assure stable operation under the unprecedented electric field of 400 V/cm which is enforced by the ALICE TPC. The GOOFIE is operating with a Ne-CO₂-N₂ [90-10-5] gas mixture as for the ALICE TPC [Gar04]. The experimental setup tests were performed at GSI.

The approach, used in this device to measure the drift velocity v_d in a gas, is given by the equation

$$v_d = \frac{\Delta l_d}{\Delta t_d} \quad (3.2)$$

where Δl_d is a known distance between two radiation sources ionizing the gas and Δt_d is a time difference in drift of electrons. The practical realization of such measurement is shown in Fig. 3.2 and is based on the measurement of the difference in drift time of electrons produced in the gas by alpha-particle tracks, at two known distances from a so-called pick-up detector. The electrons released in the gas drift down to the pickup-up detector through a constant field drift channel defined by equally spaced ring electrodes. The two single-wire cylindrical proportional counters depicted as T1 and T2 (far and near respectively) in Fig. 3.2 provide a trigger signal. The α -particles are emitted from an Americium source $^{241}_{95}\text{Am}$ with activity of 90 kBq. Both sources (S1, S2) are placed in front of the detector at well defined distances (see Fig. 3.3). These distances were calculated and measured to account for the Bragg peak produced by the α -particle in our gas. The pulseheight spectrum in the pick-up is recorded as a function of time. The pick-up detector consists of anode and cathode wires planes which are placed parallel above a cathode pad. The cathode wires are at ground potential, preserving the high \vec{E} field induced by the anode wires from entering the active drift volume of the monitor. The nominal operation voltage for the anode wires is approximately 1.4 kV. The cathode pad, of size $9.0 \times 16.8 \text{ mm}^2$, collects the signal induced during an avalanche. A newly designed pick-up detector is described in detail in Section 3.3. The voltage of the anode wire and the cathode tube of trigger counters is provided from the nearest drift field electrodes. This prevents from formations of a strong fields near the counters, and simultaneously limits the field distortions in the drift channel. Therefore, the trigger signal induced on the cathode is read through a 1.5 nF capacitor in order to decouple the read-out electronics from the high voltage of the field cage. Moreover the drifting electrons can be snatched by the field of the anode wire of the

²Gesellschaft für Schwerionenforschung mbH, Darmstadt, Germany

³Solenoidal Tracker At RHIC Forward TPC

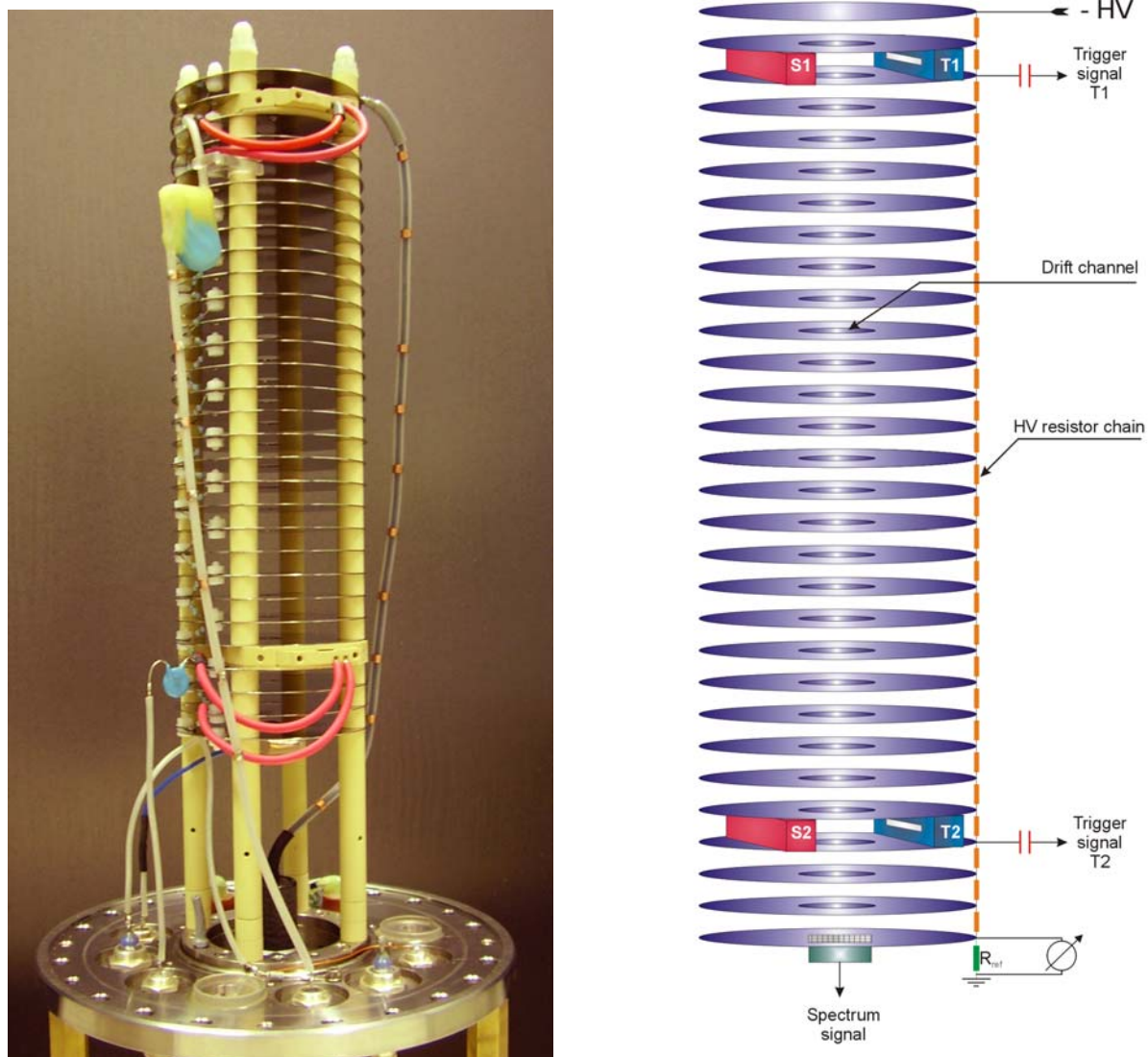


Figure 3.2: The drift velocity monitor. Right panel: the scheme of GOOFIE (T1, T2 – single-wire cylindrical proportional counters, S1, S2 – α -particles sources); left panel: a photograph with field-defining rings and two trigger detectors mounted along the drift channel.

trigger detectors. To minimize this effect, a wire-mesh has been mounted on the entrance of the counter.

The field cage is composed of 30 parallel stainless steel plates (width 0.5 mm) separated by 8.0 mm from each other. The 28 plates with a hole of $\varnothing 10$ mm in the centre provides a drift channel for freed electrons and ions. The negative high voltage is distributed between plates

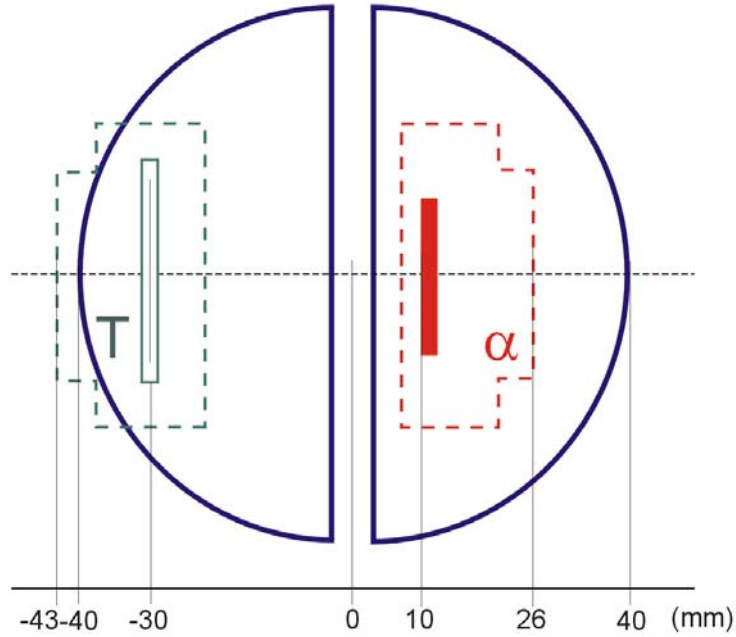


Figure 3.3: Top view of the trigger detectors (T) position with respect to the α -particles source (α). The semicircles are plastic holders for both components.

through 29 resistors. Each resistor of $2.75 \pm 0.003 \text{ M}\Omega$ is connected to the two plates via nylon screws. The field cage is inserted in a stainless steel tube which contains the inlet and outlet for the gas mixture flow and a water-cooling. The distance between the wall of the tube and the field rings electrodes is 31.5 mm, to avoid high voltage breakdowns as well as to minimize the amount of a gas in the vessel. In order to better understand the origin of the discharges which occurred in the drift monitor, viewing ports ($\varnothing 10 \text{ mm}$, $\varnothing 12 \text{ mm}$) were mounted on the main flange. The field cage is supplied with the negative high voltage of approximately -10 kV by a Heinzinger power supply PNC 20000-3 neg. The disadvantage of this power supply was that it has a significant noise due to the alternating current (AC) component remaining in the supplying voltage. Since the trigger counters are connected directly to the resistor chain of the drift monitor it was necessary to minimize AC component by introducing an external passive RC filter ($R=1.1 \text{ M}\Omega$, $C=1 \text{ nF}$). Additionally, the ability to monitor the gas temperature was increased by embedding inside the vessel two PT-100 temperature sensors at the beginning and at the end of the field cage. The sensor signals were then extracted through feedthroughs at the main flange. The **Modular Converters for Regulation Systems (MCR)** modules were used to convert the temperature measured by the PT-100 sensors into standardized electrical analog signals. The module provided a small current for the sensor (approx. 1 mA). The resulting voltage drop was amplified in the module and converted into a signal proportional to the temperature. For linearization of the resistance characteristics, the measured signal was

subsequently fed back to the input. For calibration purposes, both signals were recorded using a sampling ADC CAMAC module (LeCroy LG8252).

The results presented in Section 3.4 were obtained with the prototype read-out electronics shown in Fig. 3.4. The preamplifier-shaper cards depicted as A^{Far} , A^{Near} and $A^{Pick-up}$ were previously used as a read-out system for the CERES GOOFIE (see Section 2.4.2). The trigger logic (the discriminator and the logic fan-in fan-out (LeCroy, LRS429)) based on NIM⁴ modules provided a trigger signal for FADC module. The latter stored the pulseheight spectrum from pick-up detector. The FADC unit is a CAMAC⁵ module [Leo94] for high speed analog sampling applications. One FADC unit enables every 10 ns sampling and storing of 1024, 6 bit wide, samples into the building random access memory. For our chosen gas composition the average electron drift velocity at 400 V/cm is equal to 2.6 cm/ μ s, as shown in Fig. 3.5. This results in an average electron drift time for electrons induced by the α -particle emitted from S1 source to the pick-up detector of approximately 9 μ s. Thus, the sampling time and the storage memory of FADC module as well as the new read-out board described in Section 3.5 allows to perform the acquisition of the pick-up spectrum.

3.3 Gas Monitor Development Studies

The required drift velocity resolution of 10^{-4} by the ALICE TPC forced a further development for the gas monitors. Previously designed GOOFIE at the Max-Planck-Institut in München for the STAR collaboration does not allow for stable operation at 400 V/cm. The required electric field strength is obtained at -9860 V taking into account the monitor field cage length. The highest reached voltage within this configuration is approx. -7 kV before continuous discharge occurs. In order to better understand the origin of such behavior simulations of the GOOFIE layout were performed based on the Garfield [Vee98] application. They confirm the hypothesis that the high potential difference between the far counter and the field cage plates causes the discharges. One of the proposed solutions was to connect the anode wire and cathode tube to the nearest drift field, in order to prevent the formation of strong fields near the counters as it was described in Section 3.2. After this modification it was possible to run the GOOFIE monitor under an electric field of 400 V/cm with the electron drift length Δl_d approx. 20.4 cm. The only disadvantage of the applied solution is that the induced signal has to be decoupled from the high voltage of the field cage. Therefore the trigger signal is read through a capacitor. To avoid the discharges between the wires of the capacitor it was necessary to protect them by a layer of glue as shown in Fig. 3.2 (left panel). Moreover, the signal cable was equipped with copper rings in order to protect it from spurious discharges along the insulating surface. The same solution was applied to the HV cable increasing significantly the stability of the monitor. In order to increase the GOOFIE ability to monitor the gas temperature, which can directly improve the

⁴Nuclear Instrument Module

⁵ Computer Aided Measurement And Control

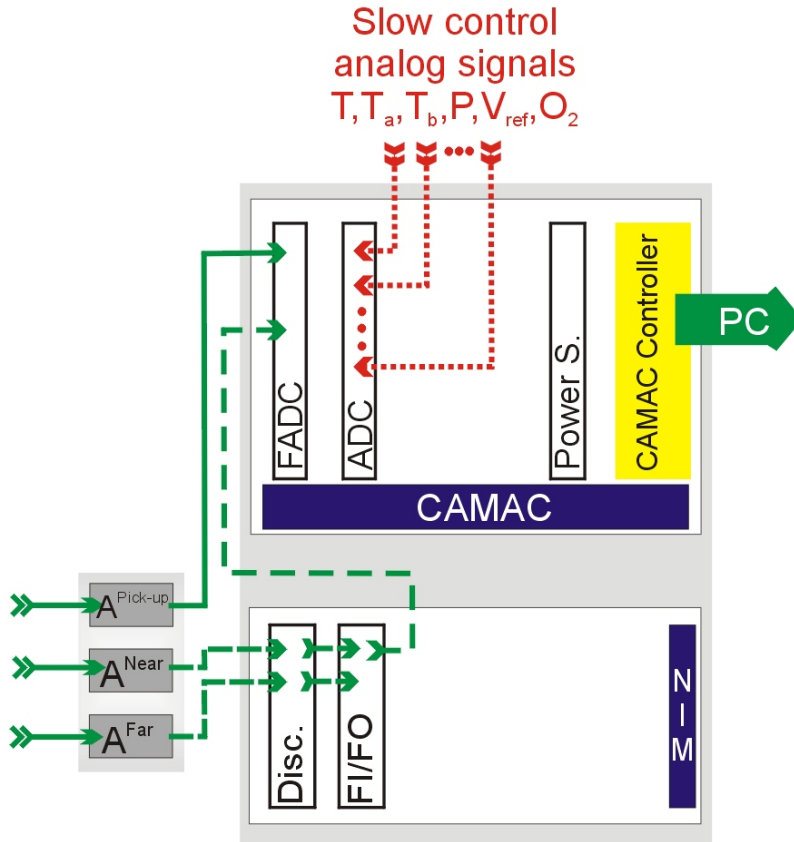


Figure 3.4: The scheme of the prototype electronic. In the NIM crate the trigger logic was build-up from the discriminator (Disc.) and the logical fan-in fan-out (FI/FO). The flash ADC module (FADC) was sampling incoming signal from the pick-up detector. The latter was supplied by the +1.4 kV from the power supply. All slow control parameters e.g. the gas temperature, oxygen contamination, pressure etc. were recording through the multichannel ADC. The CAMAC controller was connected with the PC through the PCI card.

drift velocity resolution (see Section 3.4), two PT-100 sensors were inserted into the active volume of the detector. In addition to these modifications, wire-meshes were mounted on the entrance of the trigger counters (see Section 3.2).

When a charged particle travels through matter, it ionizes the medium and deposits a dose along its path [WW02]. A peak occurs because the interaction cross section increases as the charged particle's energy decreases. The maximum of this dose is called the Bragg Peak; it occurs shortly before the particle stops due to total energy lost. Therefore, the trigger counter should be placed shortly before the Bragg peak in order to maximize its efficiency. The measurement was performed using the prototype TRD ALICE [A⁺03b] chamber with 8 pads read-

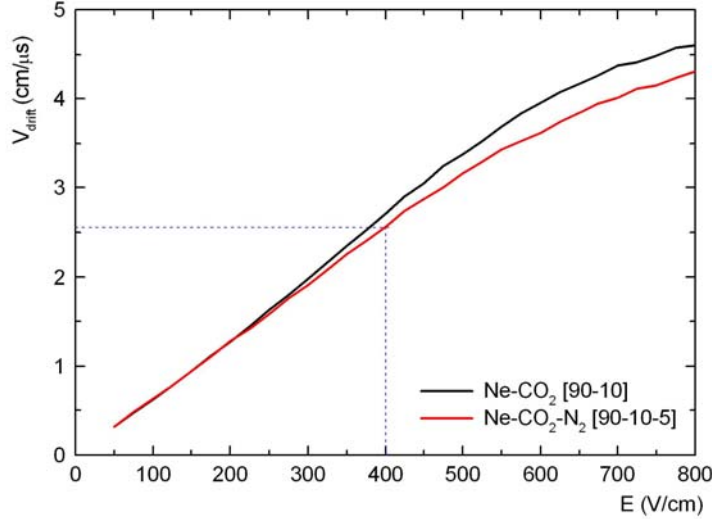


Figure 3.5: The simulation of electron drift velocity in the Ne-CO₂ [90-10] and Ne-CO₂-N₂ [90-10-5] gas composition as a function of the electric field performed by the Garfield simulation package.

out. The uncollimated $^{241}_{95}\text{Am}$ source was located perpendicular to the read-out pads. The energy deposited by α -particles was recorded for each pad using one read-out channel. Therefore, the accuracy of the measurement was folded with the width of a single pad. Additionally to the measurement, numerical calculations of the energy loss by helium nucleus of energy 5480 keV in our gas mixture were performed using the SRIM application [Zie98]. In Fig. 3.6 the ionization as a function of the α -particles range in the Ne-CO₂-N₂ [90-10-5] gas mixture is shown. The data points represent the measured value, and the lines are the simulated values arbitrarily normalized. In order to account for the charge sharing between pads which depends on the electrode geometry, the simulated data were folded with the pad response function (PRF) [GL79, Mat88] of the detector. The discrepancy between the measurement and the simulation was due to the fact that α -particles source was not collimated. Qualitatively, both methods are in agreement concerning the Bragg peak determination. The optimum separation distance was found to be 40 mm.

Previously used pick-up detector had not an uniform gain distribution (see Fig. 3.7), whereas the electric fields created by the anode wires affects significantly the drift field channel of electrons, thus smearing the arrival time of the drifting electrons. Therefore, based on the simulation performed with the Garfield software, a new pick-up detector was designed [Gar]. In Fig. 3.8 the layout of the detector together with the electric field and the electron drift lines, as well as the gas multiplication factor are shown. The new pick-up detector is composed of two

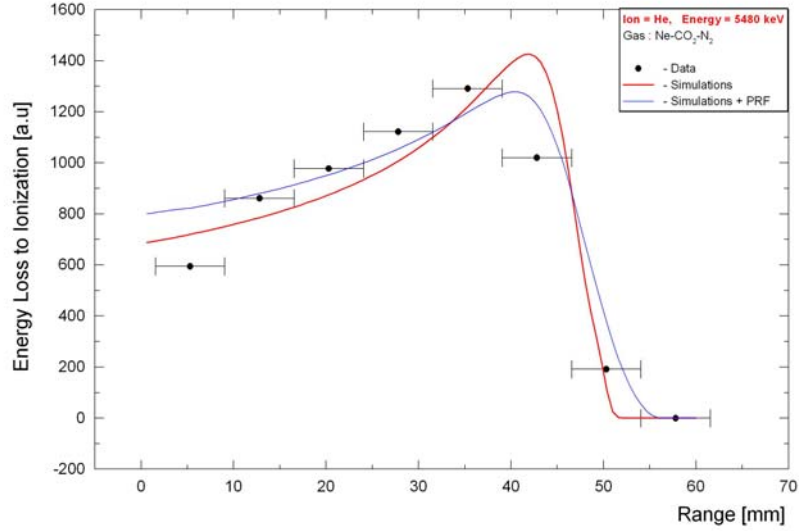


Figure 3.6: The energy deposition in the Ne-CO₂-N₂ [90-10-5] gas mixture by the α -particle emitted from an $^{241}_{95}\text{Am}$ source as a function of the distance. The comparison between the experimental results (full circle) and the simulations (lines).

planes of wires, anode and cathode, and one cathode pad where induced signal is recorded. The distance between the anode and the cathode wires plane is 2.75 mm, and between cathode pad and anode wires plane is 1.7 mm. The anode wires plane is divided into three groups, one in the center with wires of $\varnothing 25 \mu\text{m}$ and remaining two at the edge with wires of $\varnothing 75 \mu\text{m}$. The pitch between wires within the group is 1 mm, and between groups is 1.25 mm. Such arrangement of the anode wires significantly increases the uniformity of the gain and the electron arrival time in comparison with the old pick-up detector. Moreover, the disturbance of the electron drift field, caused by an electric field induced by anode wires of the pick-up detector, is significantly reduced by increased number of cathode wires. In order to reduce the charge accumulated on the external surface of the pick-up detector (the charge is accumulated close to the mounting points of the anode wires being covered by a layer of glue) the copper strips were attached to it and connected to the ground. This eliminates discharges which occurred sometimes in the GOOFIE monitor. Other origin of discharges was connected to the poor curing of the glue that was used to protect the tips of anode wires in the pick-up detector. Furthermore, similar problem - extended curing period of the glue - was recognized during the production stage of the ALICE TRD chambers[Gar]. These discharges, of frequency $14 \mu\text{Hz}$, were observed through the viewing ports installed in the main flange.

The drift velocity and the gas gain depends directly on the gas composition. Therefore,

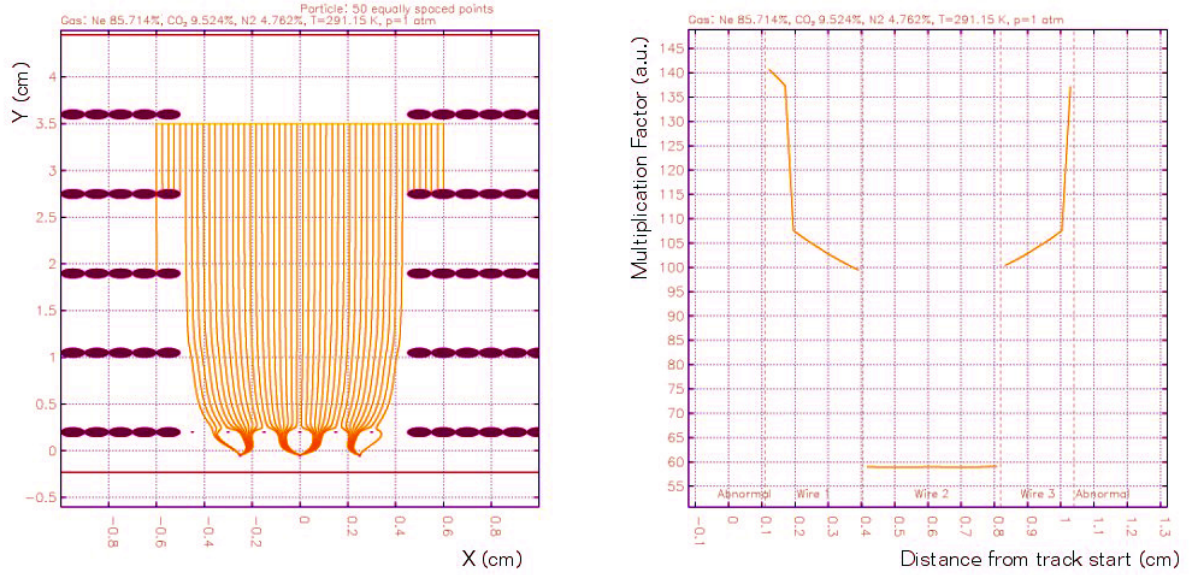


Figure 3.7: The simulation results of previously used pick-up detector. Left panel: the electron drift lines to the three anode wires. Right panel: the multiplication gas factor obtained for layout of anode-cathode wires and the pad cathode.

in order to monitor the gas mixture in the ALICE TPC, the gain and the drift velocity were simulated for a different content of the CO_2 and N_2 . The simulations performed by the Maxwell [Bia99] and the Garfield applications provided for our gas mixture two-dimensional tables of the drift velocity v_d and the gas gain G , respectively, as a function of CO_2 and N_2 concentration (see Fig. 3.9). The GOOFIE monitor provides both input values, the drift velocity and the gain, therefore after normalization with respect to the initial values of ($\text{CO}_2=10\%$ and $\text{N}_2=5\%$) it is achievable to calculate the gas composition by solving a set of linear equations

$$\begin{aligned} v_d(\text{CO}_2(\%), \text{N}_2(\%)) &= A \cdot \text{CO}_2(\%) + B \cdot \text{N}_2(\%) + C, \\ G(\text{CO}_2(\%), \text{N}_2(\%)) &= D \cdot \text{CO}_2(\%) + E \cdot \text{N}_2(\%) + F \end{aligned} \quad (3.3)$$

where, $\text{CO}_2(\%)$ and $\text{N}_2(\%)$, are contents of the carbon dioxide and the nitrogen in the gas mixture respectively. The parameters (A-F) correspond to the plane coefficients obtained by fitting the simulated two-dimensional tables which were normalized for the drift velocity and the gain to initial values. In the table 3.1 the obtained fit parameters from the normalized the drift velocity and gas gain tables are shown. Moreover, the measured variables, v_d and G , also depend on the gas density, thus both of them need to be corrected for.

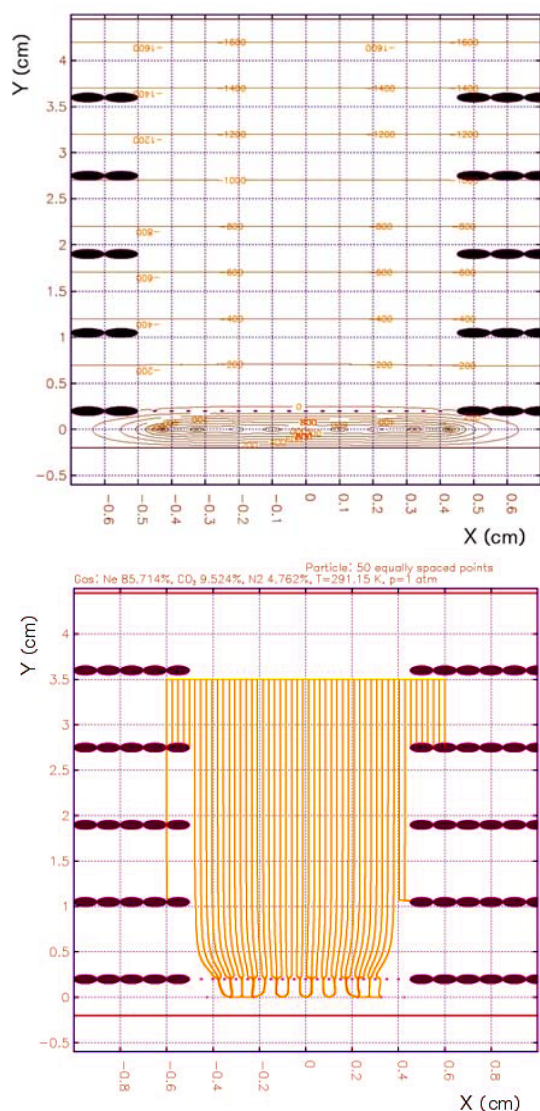


Figure 3.8: New design of the pick-up counter. Left top panel: the electric field lines. Left bottom panel: electrons drift line shows a fairly almost uniform electron arrival time. Right panel: the multiplication factor.

3.4 Data Acquisition and Analysis

After implementing all modifications explained in Section 3.3, several runs of the detector response were performed. The data acquisition and an online monitoring was based on the LabView application running under Windows. During approximately 20 minutes the pulse-height spectrum from the pick-up detector was accumulated over 2500 events recorded by the FADC (see Fig. 3.10). The slow control variables (the gas temperature inside and at the gas outlet, the ambient pressure, the oxygen contamination, and the electric field of the drift channel) were averaged over this time and stored together with the accumulated spectrum of the pick-up on ASCII file. Such file was used as an input for the offline data analysis. Moreover,

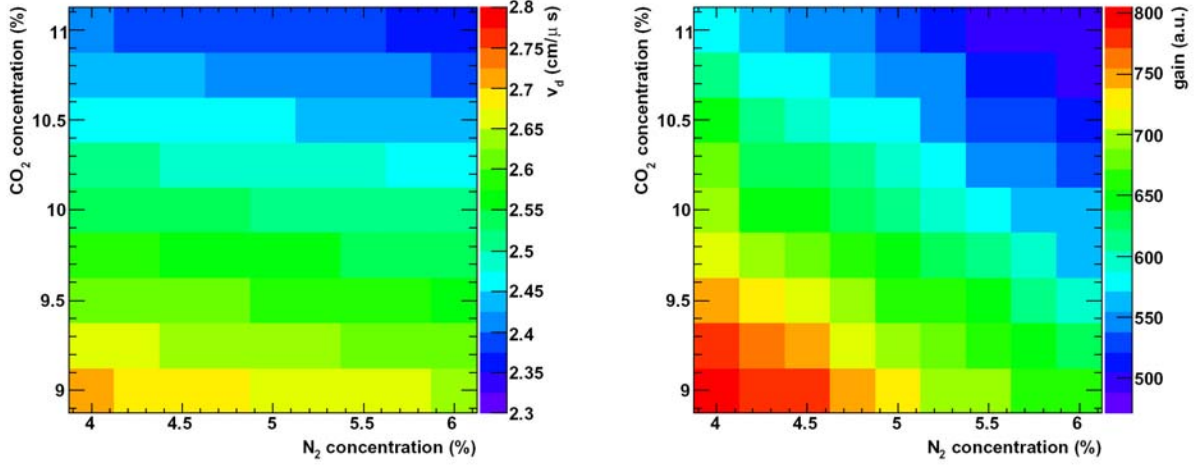


Figure 3.9: The dependences of the gain and the drift velocity as a function of CO₂ and N₂ concentration in the ALICE TPC ternary gas mixture.

parameter	value	error
A	-5.657×10^{-2}	1.72×10^{-1}
B	-9.012×10^{-3}	1.72×10^{-1}
C	1.615	1.93
D	-1.667×10^{-1}	1.73×10^{-1}
E	-1.102×10^{-1}	1.73×10^{-1}
F	3.238	1.96

Table 3.1: The plane coefficients used for calculation of the CO₂ and N₂ concentration in the ALICE TPC gas mixture.

the online application extracts the drift velocity and the gas gain from the accumulated pick-up spectrum by fitting a Gauss distributions to the peaks coming from the near and far source. The obtained values were plotted together with the slow control variables as a function of the production time. The results presented in this section were obtained with a premixed gas in order to avoid, at this stage, any possible fluctuation in the gas composition. The drift velocity is extracted from the position of the peaks in time corresponding to the signals triggered from either the near and the far detectors. Each peak, accumulated over about 2500 events, is fitted with the function

$$f(t) = f_0 + A \cdot \exp \left\{ - \exp \left(- \left(\frac{t - t_{MPV}}{w} \right) \right) - \left(\frac{t - t_{MPV}}{w} \right) + 1 \right\} \quad (3.4)$$

where, f_0 is an offset, t is the time, t_{MPV} is the peak position, and w is the peak width.

An example of the fit results to the pulseheight spectrum, integrated over 2500 events, is shown in Fig. 3.10. Also, the areas under the peaks of the integrated pulseheight spectrum are

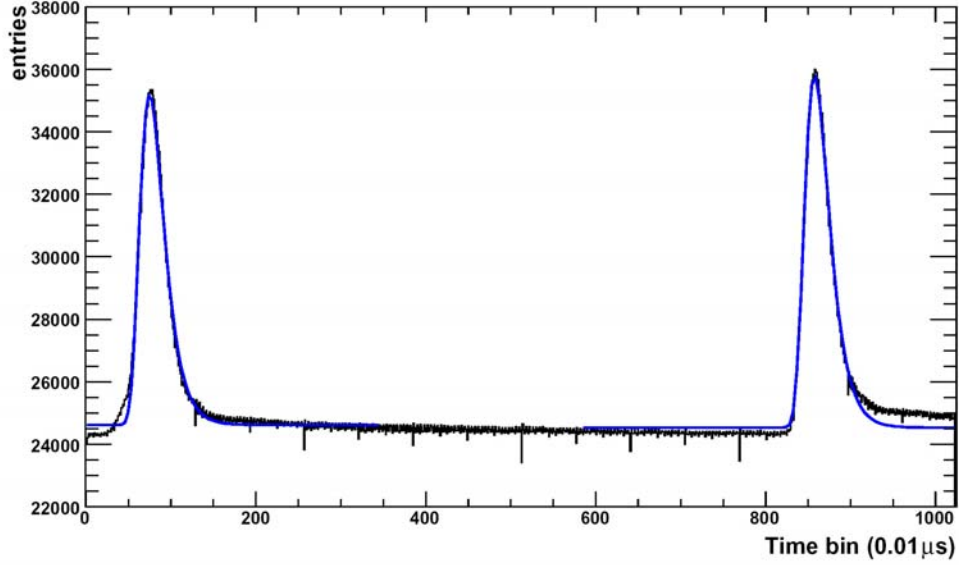


Figure 3.10: An example of the pulseheight spectrum accumulated over 2500 events. The blue solid curves are the results of the function fitting 3.4 to each peak.

extracted from the fit functions by integrating the time bins in a reasonable range around the peak position. The results obtained are normalized to the number of events which contribute into these peaks. These values, which are proportional to the gas gain, together with the drift velocity and slow control information are stored for each accumulated spectrum in a file. This file is then used as an input for the display application. The time dependence of the drift velocity, the gas density, and the oxygen contamination in the gas mixture are shown in Fig. 3.11. The steep increase in the measured drift velocity at the beginning is correlated with the temperature stabilization of the HV resistor chain (see Fig. 3.12), and partially caused by the high oxygen level at this stage. Therefore, this data subset was neglected for the calculation of the GOOFIE monitor resolution.

The influence of the pressure and the temperature changes on the drift velocity and the gas gain has to be corrected for before any analysis of the gas composition is performed. The ability to eliminate such influence is directly connected with the resolution of the gas monitor. Therefore, the accurate monitoring of the ambient condition is one of the crucial issues for the GOOFIE monitor. Assuming the precise knowledge of those variables, the drift velocity can be corrected following

$$v_{d,corr} = v_{d,raw} - P1 \left(\frac{T}{P} - \left\langle \frac{T}{P} \right\rangle \right) \quad (3.5)$$

where, $v_{d,raw}$ is the measured drift velocity, T/P is the gas density at the time of the measurement, $\langle T/P \rangle$ corresponds to the average value of the gas density (calculated over the whole time), and the $P1$ parameter is the slope of the linear function fitted to the correlation shown

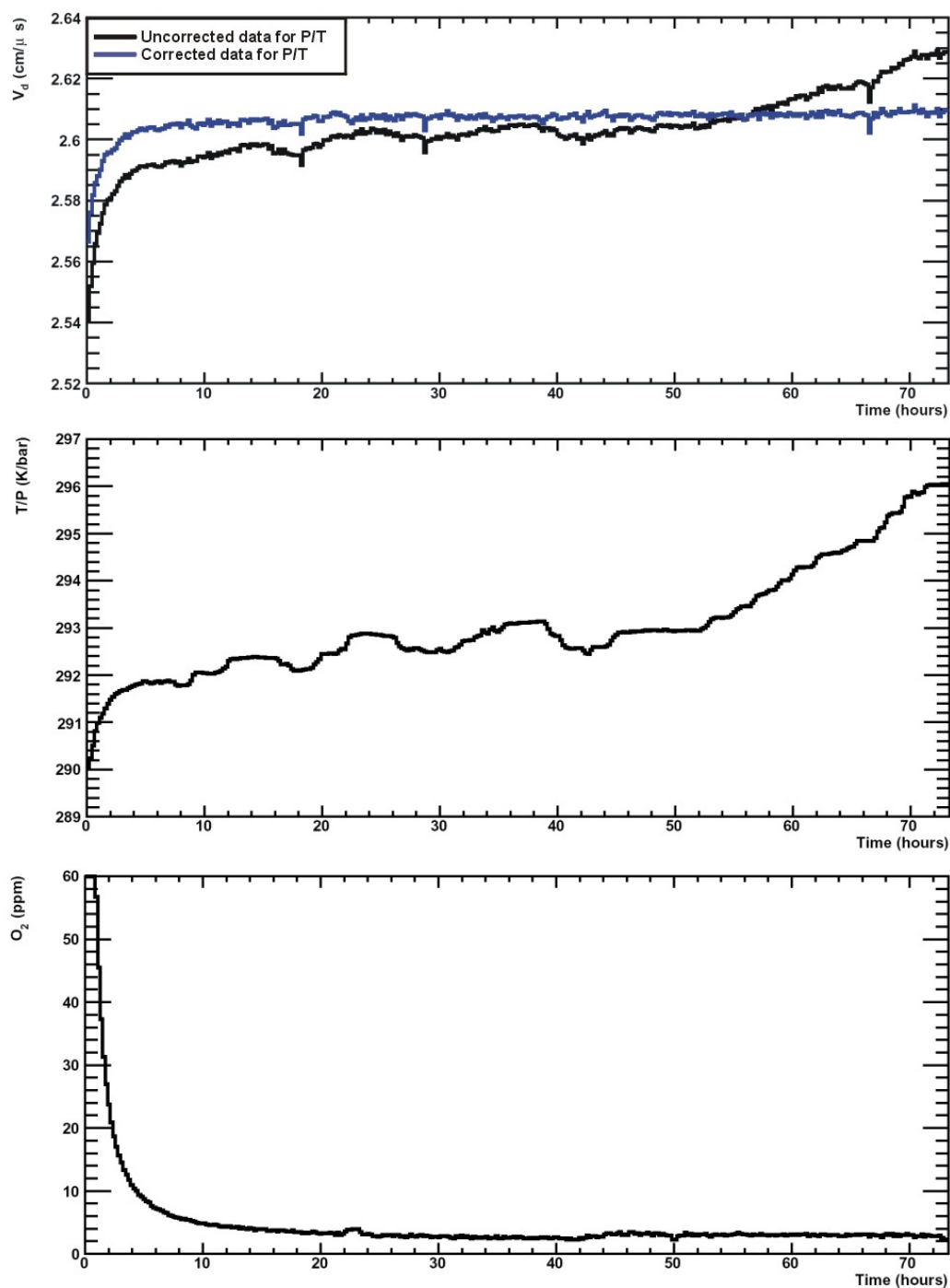


Figure 3.11: The time dependence of the drift monitor variable. Top panel: drift velocity as a function of time, the black line is the raw data, and blue line after applying the T/P correction. Middle panel: the gas density. Bottom panel: oxygen contamination.

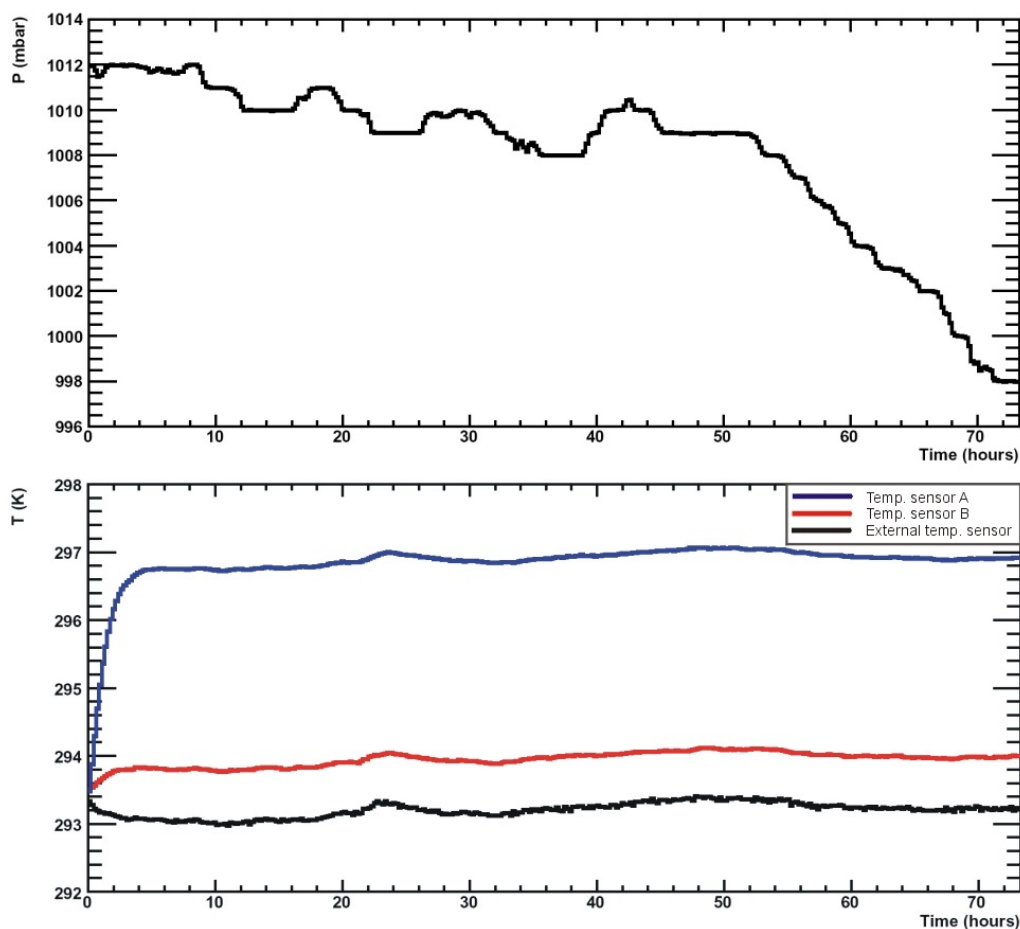


Figure 3.12: The time dependence of the pressure and the temperatures.

in Fig. 3.13. In a similar manner, the gas gain can be corrected for the T/P changes. The corrected drift velocity values are shown in Fig. 3.11 (top panel) as a blue solid curve.

A subsequent offline event-by-event analysis was also performed. This allows to investigate the following aspects

- number of events per integrated pulseheight spectrum,
- different method for the extraction of peak parameters,
- gain dependence of the gas composition,
- gas density influence on the drift velocity resolution.

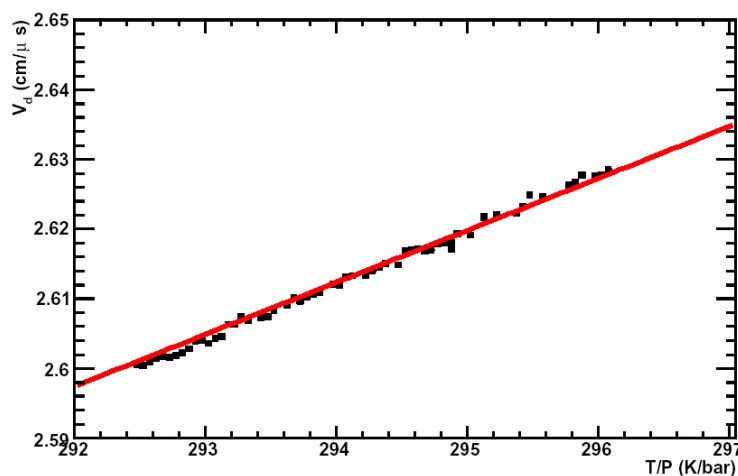


Figure 3.13: Correlation between the measured drift velocity and the gas density.

For each event the pulseheight spectrum was recorded together with the slow control information and stored in an ASCII file. Such solution is not optimized but allows one to record each individual event without significant changes in the online LabView [Ins] application. In this fashion approximately 300 thousand of events were recorded. However, to perform an efficient analysis the data set was first translated into ROOT data format [BR]. Within this framework an analysis data chain was implemented what allowed to study the different peak extraction methods, to merge different numbers of events, and to perform the drift velocity and the gas gain analysis for different events cuts. The results of this analysis answered only partially the questions mentioned above. The optimal number of integrated events was found to be about 2500 as the compromise between the statistical deviations and the ambient conditions changes. Two additional methods of the peak position extraction were also performed. The first is based on the position of the time bin with maximal amplitude, whereas in the second method each individual peak is fitted with Eq. 3.4. The extracted peak positions from the pulseheight spectra are averaged over 2500 events and the mean value is thus obtained. At this stage the different quality cuts can be applied too. From the data set prepared in this manner the drift velocity and the gas gain is extracted and stored in additional ROOT file. These files are used as an input for the offline display application. The qualitative comparison of the results from the different method of the peak extraction analysis showed that the event-by-event peak fitting procedure is a most suitable method for drift velocity analysis. However, in order to quantitatively distinguish between the different methods of peak extraction as well as to understand better the gain variation further analysis has to be accomplished. Therefore, the event-by-event analysis of the GOOFIE data was performed with the newly designed read-out electronics and the redesigned data acquisition chain (see Section 3.5).

3.5 Development of the Read-out Electronics

The prototype electronics used during the monitor response study was a collection of NIM and the CAMAC modules. In order to minimize the read-out electronics of the GOOFIE a new read-out board was developed at CERN EP/ED department [Mus05, Jun05]. In Fig. 3.14 the picture of the new read-out electronics is shown. The GOOFIE monitor provides two trigger signals and the pulseheight spectrum from the pick-up, therefore the board contains three identical input channels that process the analog signals through the electronics chain shown in Fig. 3.15. Access to the information stored on the board is through a USB port. The board is supplied by two DC power supplies that deliver +5 volts for analog and digital circuit respectively. It uses the front-end ALICE TPC read-out components: the **PreAmpShaperAmplifier (PASA)** and the **ALICE TPC Read Out (ALTRO)** chips to process the analog signal. The PASA is a charge sensitive amplifier followed by a semi-Gaussian pulse shaper which has a conversion gain of 12 mV/fC with an output dynamic range of 2 V. The produced pulse has a rise time of 120 ns and a shaping time (FWHM) of about 200 ns. After the PASA, a 10-bit ADC integrated

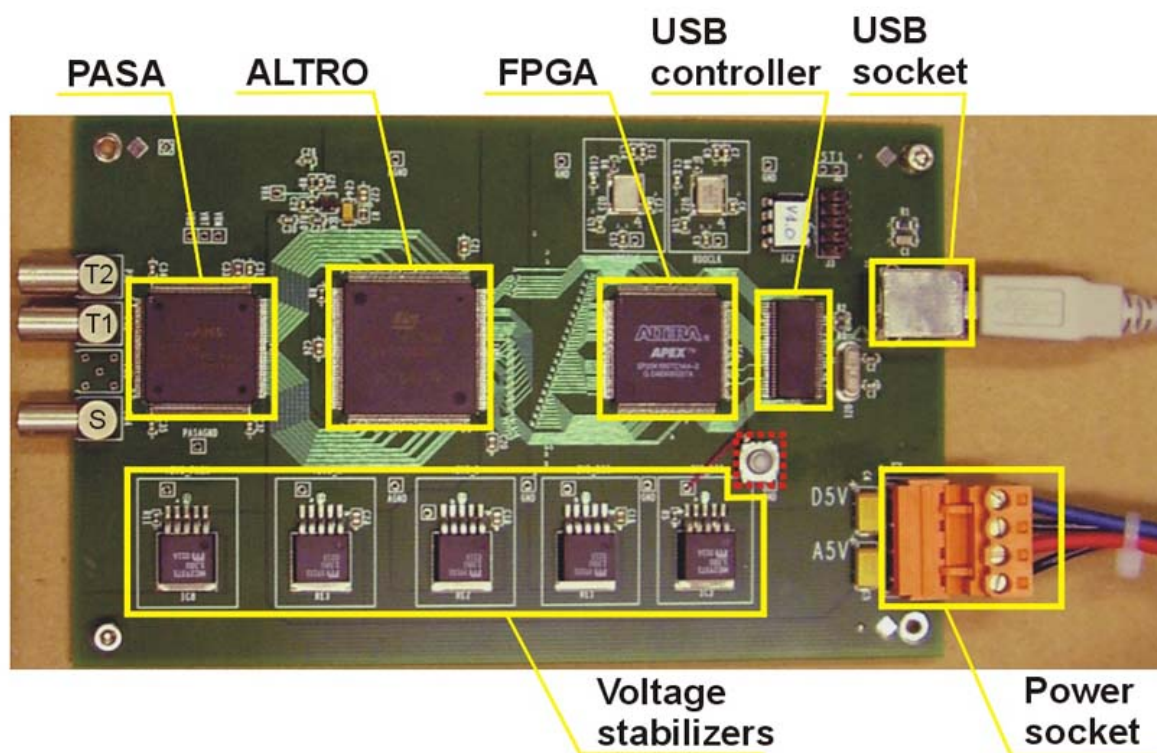


Figure 3.14: A picture of the new readout board for the GOOFIE monitor together with a short description of the components. The configuration of this board is similar to the front-end electronics of the ALICE TPC.

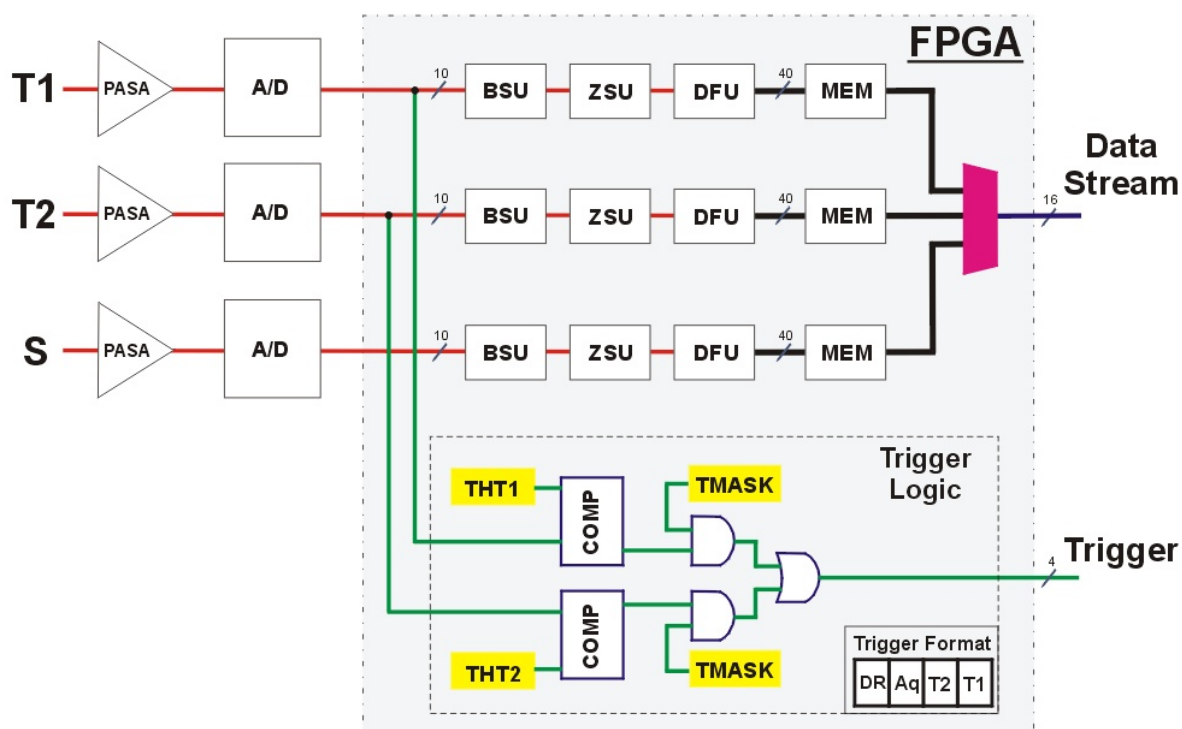


Figure 3.15: The block diagram of the new board constructed for the GOOFIE (see text).

into the ALTRO chip provides the analogue to digital conversion [CE02]. The digital signal is sent to the FPGA where processing chain units of the ALTRO chip were implemented together with the trigger logic. Originally the ALTRO provides all algorithms necessary for the signal processing (tail cancellation, base line restoration, zero suppression, etc.). First, the signal is corrected for the long-term components of the pulseheight spectrum and then the baseline is restored (BSU). In the next step, the zero suppression (ZSU) and the data forming (DFU) are performed. After a trigger occurrence the signal is stored in the memory unit (MEM). The BSU allows to remove systematic effects from measured signal by subtraction of the spurious ones. In order to perform such operation the pattern (pedestal) memory is used. Every time the chip starts an acquisition, the values stored in pedestal memory are subtracted from the measured signal, thus removing systematic perturbations. It is foreseen to use this unit to remove entirely the noise originating from the power supply. Also a fixed value (ZSPED) can be subtracted from the incoming signal. A test mode allows to monitor the pattern in the memory. The choice between different modes is selected through the board register BSLCT described in table 3.2. After the BSU the data reduction based on the zero suppression method is performed in the ZSU. In order to distinguish between the pulse from the noise a fixed threshold is applied (ZSTHD). All samples below this level are rejected, while a sample above the threshold is

Register	Description	Range
BSLCT	Pedestal subtraction modes, signal - fix value (fpd), pedestal memory (pmem) - fpd, signal - pmem	0, 3, 5
ZSPED	Fix pedestal value	0-512
ZSCTL	Zero suppression mode	(see text)
ZSTHD	Zero suppression threshold	0-512
PRTRG	Pre/Post trigger sample	0-9
NSEVT	Maximum number of samples	500
TMASK	Trigger mask; only trigger from T1, only trigger from T2, or both	1, 2, 3
TATHD	Trigger threshold for channel T1 (THT1)	0-512
TBTHD	Trigger threshold for channel T2 (THT2)	0-512
TRGEV	Trigger information	(see text)
ACTCH	Not used	

Table 3.2: The list of registers used in the GOOFIE read-out board.

considered as a start of the pulse. Additionally, the glitch filter was introduced to check for a consecutive number of samples above threshold in order to confirm the existence of a real pulse. The so-called `seq-mask` can vary from 1 to 3 samples per cluster. In order to keep enough information for further extraction, the complete pulse shape must be recorded. Therefore, a sequence of samples (pre-samples) before the signal overcome the threshold and a sequences of samples (post-samples) after the signal returns below the threshold are also recorded. The number of pre-samples and the number of post-samples can vary independently in the range between 0 and 4. The mode of the glitch filter and pre-samples, post-samples is controlled by a 7 bit register called `ZSCTL`. The bits 6-5 corresponds to `seq-mask`, 4-2 are responsible for post-samples and remaining two for pre-samples. After the zero suppression unit, each found pulse has to be tagged with a time stamp. Otherwise the timing information would be lost by removal of a variable number of samples between accepted pulses. Besides that, in order to distinguish the sample data from the time data an extra word is needed. The latter represents the number of words in the set. Such procedure is performed by the **Data Format Unit (DFU)**. Moreover, the 10-bit words of the data pulses, the time stamp and the number of words in the set are packed in 40-bit words. A trailer completes the data packet, which is the last 40-bit world of the data structure and is composed of the total number of 10-bit words and the channel address. In Fig. 3.16 the back linked data block is shown. The recorded data block is stored in the local memory (MEM) in the FPGA. When a trigger occurs the data is sent, in 16 bits words, to the USB controller and further to the PC through the standard USB 2.0 protocol.

The trigger information is obtained from channels T1 and T2 which are connected to the trigger counters in the GOOFIE. Induced signals in the counters are processed through the trigger logic implemented in the FPGA chip as depicted in Fig. 3.15. The trigger logic permits

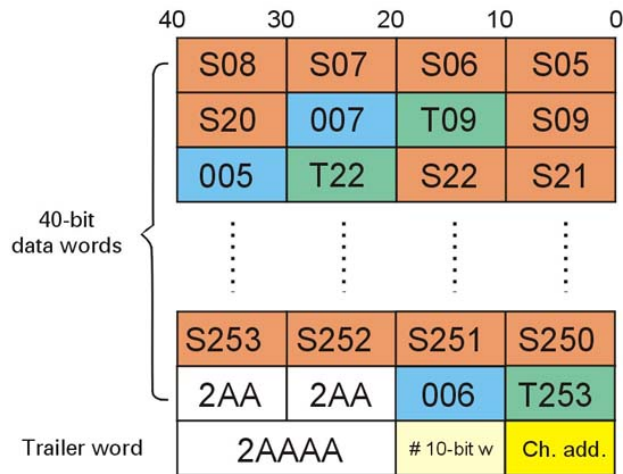


Figure 3.16: The data format of the GOOFIE board. The data are organized in 40-bits words ended with the trailer word. The pulseheight spectrum is sampled in bins of 50 ns and each found peak (S) is tagged with two 10-bit words containing time position (T) and number of 10-bit words in the set.

to set an individual threshold for each trigger channel (THT1, THT2). Moreover, it allows to select a channel which will serve as a trigger signal by register TMASK (see table 3.2). The format of the trigger is a four-bit word containing the information about the origin of the trigger (bit 1-0), the data acquisition (bit 2) as well as the information whether the data is ready to be read from the board (bit 3).

The information exchange with the board is through the USB port, therefore a specific USB driver is required for any operating system. It was possible, after some modifications, to use the USB driver originally designed for the RCU of the ALICE TPC [G⁺05], working under the Linux operating system. The modifications were performed at CERN PH-ESS division [Joo05]. Since the driver provided only a low level of functionality it was necessary to design an additional framework in order to perform the data analysis efficiently. The basic objectives of this framework were

- automatic initialization and termination of the connection with the board,
- access to the registers and pedestal memory,
- unpacking of the data,
- recording and displaying of the pulseheight spectrum for all channels,
- data acquisition,

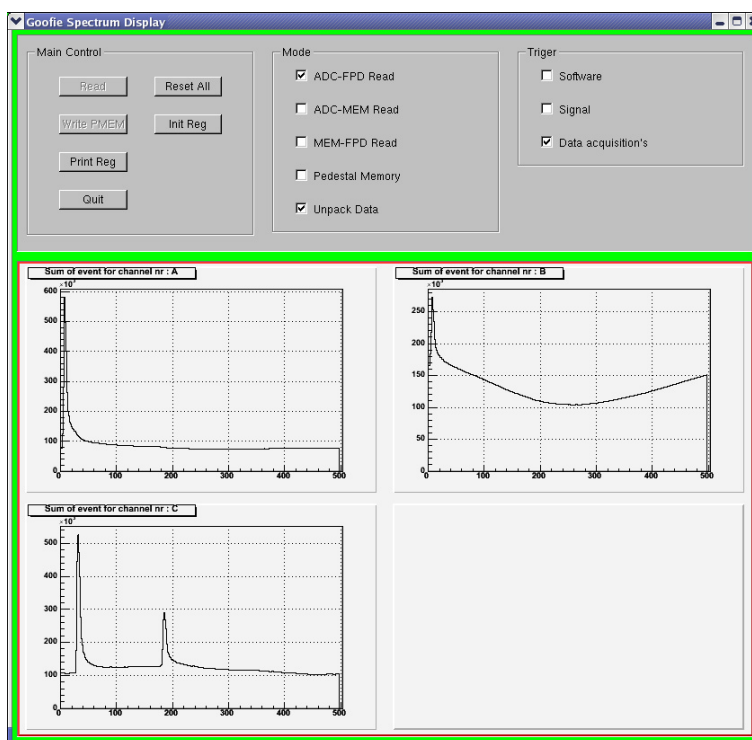


Figure 3.17: The GOOFIE display application panel.

- additional functionality for tests.

This has been implemented in the C++ programming language. The tasks were divided between four main classes. Three of them represent a group of code which can be implemented into any framework in order to process the data exchange with the board, e.g. the GOOFIE DIM server which is foreseen to be a part of the implementation into the DCS of the ALICE TPC. The last class provides a graphic interface for visualization of the incoming data. It is based on ROOT GUI classes and was implemented in order to better understand the new read-out board of GOOFIE monitor. In Fig. 3.17 the display panel is shown together with the pulseheight spectra, integrated over 2500 events, derived from triggers (channels A and B) and pick-up (channel C) detectors of the GOOFIE read-out board. The newly designed framework allows to collect individual events in an efficient way, thus opening a broad flexibility for detailed data analysis. Several runs were performed with the new read-out system and the designed framework. The results of one example are presented in [Her06]. During this run the premixed gas composition was used in order to compare the drift velocity resolution with previous results. The monitoring of the slow control variables was performed by the LabView application under the Windows operation system. The off-line analysis of this data set were performed in a similar manner as the raw data analysis obtained with the prototype electronics (see Section 3.4). Moreover, the gas composition analysis performed on the subset of these data shows irrefutably that the

GOOFIE monitor is sensitive to changes in the gas composition.

3.6 Results and Discussion

With all modifications explained in Section 3.3 being implemented, the GOOFIE gas monitor can be operated under the unprecedented high electric field of 400 V/cm, as in the ALICE TPC. The monitor resolution can be calculated as the ratio between the width of the drift velocity distribution and the mean peak position assuming a Gaussian shape. The drift velocity distribution obtained with the prototype read-out electronics together with the Gaussian fit is shown in Fig. 3.18. The obtained drift velocity resolution of 3×10^{-4} is close to required one (10^{-4}) but still above it. In order to improve the resolution of the monitor an active cooling system is foreseen to be implemented in the final version. Moreover, it can be possible to minimize the data acquisition time, now about 25 minutes per point, by modifications of the trigger counters. The results of the data collected with newly designed read-out electronics presented in Section 3.5 confirmed that the method of measurement the gas composition in the ternary mixture of the ALICE TPC with the GOOFIE monitor is efficient and sensitive to the small variation of the individual components of the mixture. Slightly worse resolution of 0.5 ‰ obtained for this setup can be attributed to the longer time of the data acquisition process, caused by the stronger influence of the baseline fluctuation seen by the far trigger. Moreover,

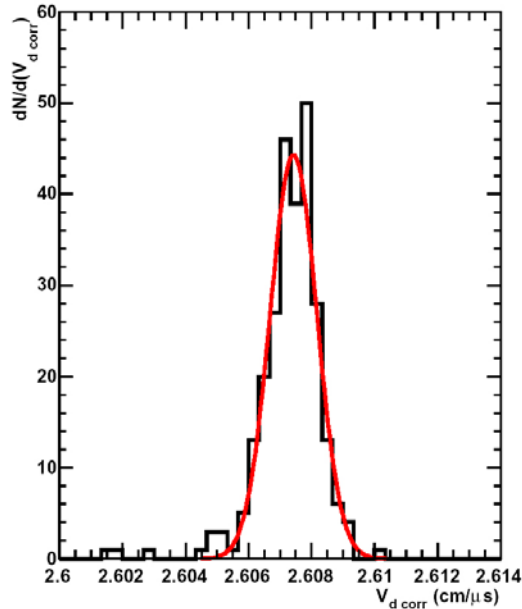


Figure 3.18: The corrected drift velocity distribution fitted by Gaussian obtained with the prototype read-out electronics. The derived drift velocity resolution is 0.3 ‰.

a pulseheight spectrum from the pick-up detector is sampled with a larger time intervals than the previous read-out electronics. Also, the peak shape of the obtained pickup spectrum differ from the previously used parameterization. Therefore, the elimination of the background induced by the high voltage power supply from the signal distributions, better monitoring and controlling of the detector temperature and decreasing the acquisition time should results in a better monitor resolution.

Chapter 4

Analysis of the CERES Data

The present high energy physics experiments are complex systems consisting of many subdetectors. Extracting meaningful numbers from the subdetectors and direct using them for any kind of physical analysis is a tedious task. Before any physics analysis can be performed, the raw data have to be converted to more convenient data format. During this process, called `production`, the compressed raw data is decompressed and the ADC values are transformed into detector hits. At this stage usually the calibrations of the recorded data can be performed. The data are corrected for effects like environmental changes, imperfections of the detectors, gas composition, beam fluctuation, etc. Afterwards hits are grouped into tracks, and are fitted to extract the momentum information. After this step, information for physics analysis becomes available. The CERES `production` chain can be presented as follows

- `step0` – first scan of the raw data, determination of the positions and widths of peaks in TDC and ADC spectra
- `step1` – second scan of the raw data, collecting calibrations information
- `step2` – third scan of the raw data, application of the calibration and data reduction
- `step3` – scan of the `step2` output data, further calibrations and data reduction.

The C++ COOL (Ceres Object Oriented package Library) was an integral part of the CERES data analysis chain. Since the COOL package is a very complex and has a sophisticated structure, this framework was not suitable for the efficient physical analysis. In order to facilitate and speed up experiment analysis, a new data format and the essential analysis framework has been designed (see Section 4.3). The first three steps of the analysis were performed in the COOL framework. The output format of `step3c` was designed to minimize the data volume for the subsequent physics analysis.

The `step3` production and all the calibrations described in this section were performed as a part of this thesis work.

4.1 Run 2000

In 2000 the CERES experiment collected a sample of about $33 \cdot 10^6$ Pb-Au collision events at 158 GeV per nucleon. Majority of this data sample was recorded triggering on the most central 7 % of σ_{GEOM} ; additionally, approx. $3 \cdot 10^6$ events with 20 % of σ_{GEOM} and about $0.5 \cdot 10^6$ events with minimum bias trigger were taken. For the calibration purposes, short runs were recorded with the laser tracks, lowered beam intensity, without the target, and without magnetic field. The complete list of the runs taken in the year 2000 can be found in [Miš00]. The SPS accelerator provided ions beam as 4 s bursts every 19,2 s with typical beam intensity of 10^6 ions per burst. Each recorded file corresponded to one burst. The recorded data was stored at the CERN Advanced **STOR**age Manager – CASTOR [B⁺05]. The $\sim 10^5$ bursts were organized in groups (units) of ~ 200 to facilitate calibrations. One calibration unit, thus, corresponds to about 1 hour of data taking.

4.2 Production

The `step0` to `step2` were combined into the large scale `production` of the CERES raw data set [Yur06]. It was performed at the Batch Farm of the CERN Computing Center and took approx. 2 months. During this stage the raw data collected from each detector was unpacked in order to recover the original time sequence of the signals. Such unpacked data, together with the information about the detector calibration stored in the **Start Of Run** – SOR file, was used to fill the lists of the pixels for a given subdetector with the amplitudes and time information.

In the presented analysis of the two particle correlations mainly information from TPC was used, therefore only for this subdetector the short description of the data reconstruction chain is presented. More detailed information about the data reconstruction for all subdetectors can be found in [Yur06, Lud06].

The total number of the spatial pixels in TPC is close to 4 millions. Such large number of pixels taking into account the number of event recorded by the CERES experiment, requires a fast and an accurate algorithm for the track reconstruction. To accomplish this goal the task was organized in the three following steps

- **TPC Hit Finding** – A hit is defined as a local maximum of the amplitude for a given pad and a given time bin. To identify a local maximum the pad and the time coordinates of the pixels were stored in the two-dimensional array and afterward scanned in azimuthal and then in radial direction. The criteria applied during this scan allow to suppress artificial peaks originating from the noise fluctuations. In the case of the amplitude values equal over an odd number of pixels – a middle one is chosen, whereas for an even number of pixels – the amplitude value of the neighboring pixels is used and a pixel with a

neighbor having bigger amplitude is chosen as a local maximum. The signal induced by the particle is usually shared by three pads (see Section 2.4.2) which correspond to 3 pixels in pad direction and approx. 5 in the time direction. Therefore, in order to calculate the position of a hit a center of gravity in ϕ and time direction is derived in a frame of 3 pads \times 5 time-bins around a local maximum called a hit-area. To cope with the overlapping hit-areas each pixel in a frame is weighted with the sum of the adjacent local maximum amplitudes. The hits derived in the pad-time coordinates are transformed to the Cartesian coordinate system with the help of a lookup table which absorb the whole transport process of the charge clusters in the electric and magnetic fields inside the TPC.

- TPC Track Finding – Reconstructed hits are combined into the tracks. The maximum number of hits per tracks is given by the number of TPC planes (20). The minimum of 6 hits was required in order to reduced the numbers of artificial tracks. The procedure to find a track is based on the so-called candidate hit with a z-position around the centre of the TPC. Afterwards, from the four subsequent planes (2 upstream and 2 downstream) the four hits closest to the candidate hit are chosen and next all five hits are combined and the sign of the track's curvature in ϕ direction is found. This information is used to define a ϕ window in which further hits are searched. In the next step a linear extrapolation is used to find another hit position in ϕ direction and the procedure is repeated until no more further hits are found. Subsequently, a second order polynomial fit with the Tukey weights [MT87] is used to find the hits omitted during the first iteration. In the case of the soft tracks, which are of a great importance for the dilepton analysis, even more sophisticated algorithms were applied [Yur06].
- TPC Track Fitting – Information about the kinematical properties of the reconstructed tracks are accessible only with the help of a Monte-Carlo simulations. Due to an inhomogeneous magnetic field of the CERES TPC analytical description of the particle trajectory was not possible. Thus, a collection of reference tracks generated with the magnetic field map is used for the momentum calculation. The reference tables used for the track fit in the $\phi - z$ and $r - z$ planes were generated using the GEANT simulation [B⁺87] of the CERES experimental setup. The generated hits were stored for a classes of the track inverse momentum, polar angle, and azimuthal angle. For each reconstructed track a straight line in the $r - z$ plane was fitted and then an azimuthal deflection of the track was derived from the fit of two different functions with 2 or 3 parameters. The two-parameters function assumed that the track has an origin at the vertex and provides the radial offset and the inverse momentum of the track, whereas the three-parameters fit additionally takes into account the multiple scattering. Since the low momentum tracks are much more affected by the multiple scattering the three-parameter fit better describes their momentum. For tracks with the momentum larger than approx. 4 (GeV/c) the two-parameters fit has a better resolution due to the additional vertex constraint. In order to take advantage of both parameterizations a weighted combination is provided. Due to

the multiple scattering in the RICH2 mirror and the magnetic field generated by the TPC coils an incoming particle can be distorted before it will reach the TPC active volume. Therefore, the track orientation was an extrapolation to the RICH2 mirror position.

The tracks reconstructed in this manner, after further calibrations explained in the following sections, were used for the two particle correlations analysis.

Monitoring of the quality of the reconstructed data was an integral part of the `production` chain. The monitoring of the `step2` data was accomplished by histogramming the most important variables and fitting them in order to extract the quality parameters. The monitored quantities were organized in five groups

- Trigger – information about the event and the slow control parameters
- Silicon Detector – monitoring of the silicon drift detectors
- RICH Detector – performance of the RICH detectors
- TPC – information about reconstructed hits and tracks from TPC
- Correlations – matching characteristics between subdetectors, etc.

For each unit three groups of 10 bursts, selected from the beginning, middle, and the end, were monitored. The obtained quality parameters were visualized using `cermon` application [Ant04b]. The results could be plotted vs. the data taking time or vs. the data analysis time, thus helping to track the origin of changes in data quality.

4.3 Data Reduction (step3c)

The output data volume of `step2`, explained in Section 4.2, was still too large for an efficient physics analysis and thus further data reduction was required. This was achieved in `step3c` which stored only those variables which were needed for physics analysis. The output of this step was stored in ROOT tree format (Appendix A). The information from each stored event was divided into two main classes, the event (`CSEvent`) and the track (`CSTrack`). The `CSEvent` class contained the information which allows to characterize the event like the collision vertex, the multiplicity, the production time, the trigger properties, and the reaction plane orientation, as well as the array of tracks recorded by all the subdetectors. Each `CSTrack` contained a TPC track segment and the information from the closest tracks of the remaining subdetectors. Closest tracks were found based on the opening angle calculation. Only for the SDD non-vertex tracks a custom matching algorithm was used [Lud06].

production name	average cpu time per event (sec)	total number of produced events 10⁶	total size in (TB)
prod012_01	2.2	21.6	0.90
prod013_00	2.2	7.9	0.34

Table 4.1: Performance of the step3c production. The two numbers contained in the name denote the version numbers of the step0-2 and the step3 productions, respectively, e.g. prod012_01 means the data were processed with the version 12 of the step0-2 chain, and subsequently with the version 01 of step3.

The step3c was performed at the CERN Batch Farm and took approx. 2 weeks. All production components were implemented using C/C++ programming languages. Table 4.1 shows the performance of the step3c. The available data set was divided into groups of five units. For each such group a file with the setup information was created. The production chain was using these files as an input and processing the files as follow

- transferring the step2 output files from the CASTOR tapes to the pool via Remote File I/O (RFIO) protocol,
- executing one batch job for each ten step2 ROOT files,
- storing the reduced events in the new step3c ROOT file,
- collecting a trigger information from the step2 ROOT files for the centrality calibration (see Section 4.8) purpose,
- storing a momentum calibration information,
- grouping ten step3c ROOT files into one tar file in order to avoid an overloading of the CASTOR system with a high number of the small size files,
- transferring a tar file to the CASTOR tapes,
- copying the output of the momentum calibration files on the AFS volume.

Prior to the data reduction the event vertex refitting procedure and TPC tracks refitting were performed. The event vertex refitting procedure was used for final tuning of the vertex position. In the step2 it was already clearly visible that the reconstructed vertex positions were not in agreement with the physical position of the 13 gold discs. Therefore, in the step3c the event vertex refitting procedure was implemented. In this procedure the radius of the reconstructed hits was recalculated using the correction values. The obtained hits were combined into tracks and from them the new event vertex was calculated. In Fig. 4.1 the distribution of the reconstructed vertex positions is shown. Thirteen gold discs were well resolved along the

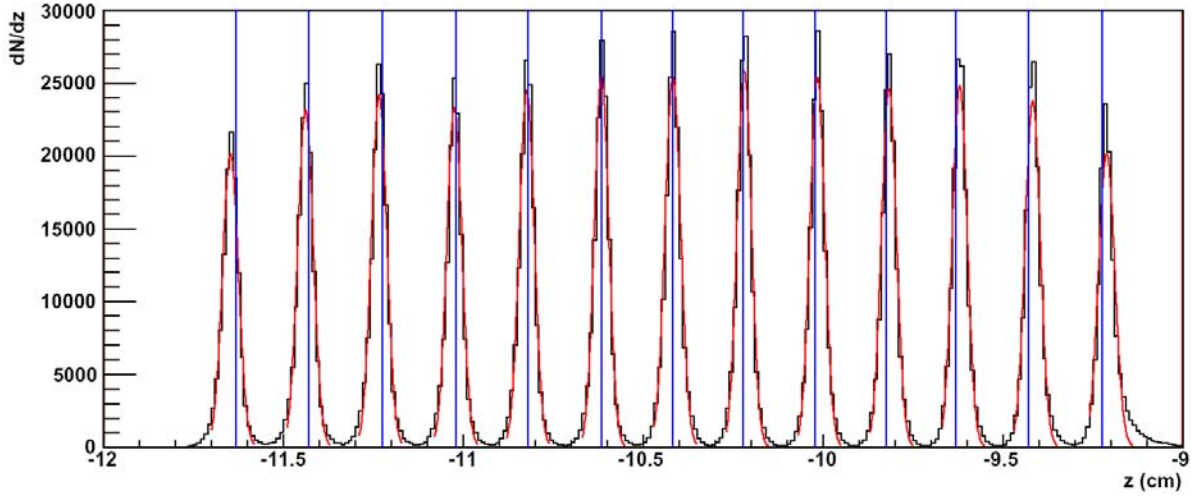


Figure 4.1: The reconstructed vertex position along the beam axis after applying the vertex refitting method. The physical position of targets are depicted as horizontal solid lines.

beam direction with a resolution of approx. $210.0 \mu\text{m}$. On the other hand, in order to improve the momentum resolution, the position of TPC hits was calibrated using the high momentum π tracks. This procedure was implemented in the `step3c` and called TPC tracks refitting. Also, trigger information (scalars) were collected in order to properly calibrate the centrality of the collision (see Section 4.8). The data quality was monitored, similar like for `step2`, by histogramming the most important variables separately for each data unit. The access to the monitoring information was provided through the `cermon` application [Ant04a] from the GSI Linux environment.

4.4 Momentum Calibration

The momentum resolution of the TPC is determined by the spatial hit resolution, the number of reconstructed hits on tracks, and the multiple scattering in the active volume. In order to estimate quantitatively the momentum resolution of the CERES TPC, a full tracking simulation was performed [Yur06]. The differences between the original and the reconstructed momenta defined the momentum resolution as the standard deviation of the derived distribution. The track fitting algorithm allows to use the two- and three- parameterizations of the track curvature. The two-parameter fit (p_2) yields optimal results for high momentum tracks, while the three-parameter fit (p_3) describes better low momentum tracks. A combination of both fitting methods was used for best momentum resolution over the whole momentum range. The

relation between the combined momentum track p_{comb} and p_2, p_3 is given by

$$p_{comb} = \frac{(p_2/\sigma_2^2) + (p_3/\sigma_3^2)}{(1/\sigma_2^2) + (1/\sigma_3^2)}, \quad (4.1)$$

where σ_2 , and σ_3 are the relative momentum resolutions of a given momenta obtained for the two- and three-parameter fit, respectively. The momentum resolution obtained with the final calibration is

$$\frac{\Delta p}{p} = 2\% \oplus 1\% \cdot p/\text{GeV} \quad (4.2)$$

resulting in $\Delta m/m = 0.038$ for the ϕ meson.

The absolute measured value of a particle momentum can vary during the data taking period. It is caused by the fluctuation in the electric and the magnetic field, the change in the gas composition, the temperature, and in the ambient pressure. Calibrations applied to account for these effects in some cases are not sufficient to remove them entirely. This leads to smearing of the reconstructed momentum. Assuming the equal abundances of positively and negatively charged particles and the infinite spatial and temporal resolution of the detector, the distribution of the charge over momentum (q/p) should be centered at zero. The residual miscalibration, discussed above, can manifest itself as a shift of the q/p distribution, as depicted in Fig. 4.2. Therefore, further calibrations of the reconstructed momentum have to be performed. A convenient particle choice for this purpose are pions, due to similar multiplicities of π^+ and π^- . The nominal minimum position of the q/p distribution was found by comparing the reconstructed masses of Λ^- and $\bar{\Lambda}$ -hyperons in the data as a function of momentum. The systematic variation of the q/p minimum position was quantitatively parameterized by

$$F(q/p) = F(0) + P1 \cdot (q/p - q/p_{min.pos.})^2 + P2 \cdot (q/p - q/p_{min.pos.})^4, \quad (4.3)$$

where $F(0)$ is an offset of the q/p minimum position ($q/p_{min.pos.}$), $P1$ and $P2$ are the slopes of the q/p distribution. In Fig. 4.3 the position of the minimum of the raw q/p_{comb} distributions, obtained for pions sample identified via the energy loss vs. momentum in the CERES TPC, are shown as a function of the unit number. The difference between the nominal value and the one extracted from the fit is used to correct remaining deviations in the reconstructed momentum.

The calibration was done in the three major steps. In the first step, the necessary information was collected during the data reduction process (`step3c`) for each calibration unit. Based on the information from RICH detectors the high momentum pions were identified by the ring radius and afterwards matched with the remaining SDD-TPC tracks. The momenta of the found pion tracks were stored in two-dimensional histograms of $n(q/p, \phi_{TPC})$ for a given bin of polar angle (θ_{TPC}). This allows to account for the geometrical effects and the limited knowledge about \vec{B} and \vec{E} fields. The optimum bins were found to be 43.5 mrad for the azimuthal angle and 20 mrad in the polar angle. The recorded two-dimensional histograms were merged in three groups of subsamples: for positive \vec{B} field at the beginning of the beam

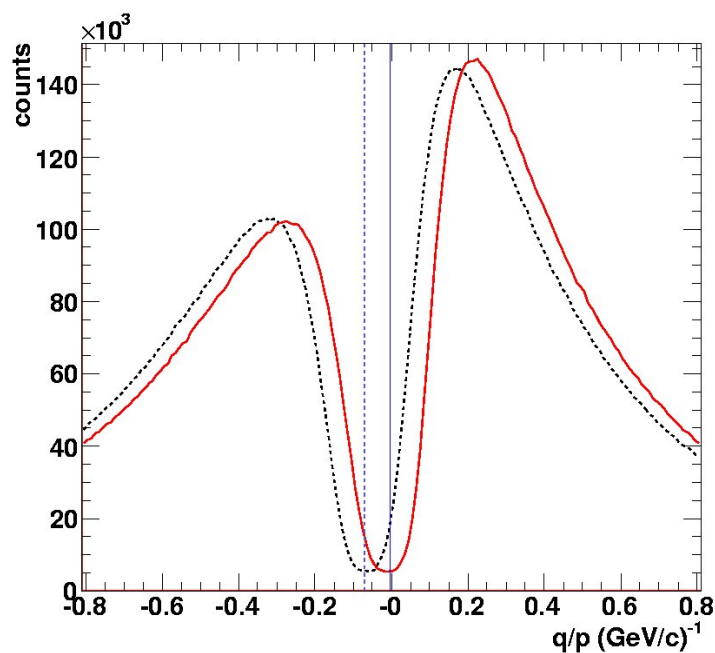


Figure 4.2: Sketch of the calibration method for small momentum variation. The solid and the dash curves correspond to the nominal and the measured positions of the inverse momentum distribution, respectively. The amount of displacement in the (q/p) -direction is used as an additive correction to $(1/p)$.

time, negative \vec{B} field, and positive \vec{B} field at the end of the beam time. The correction factors

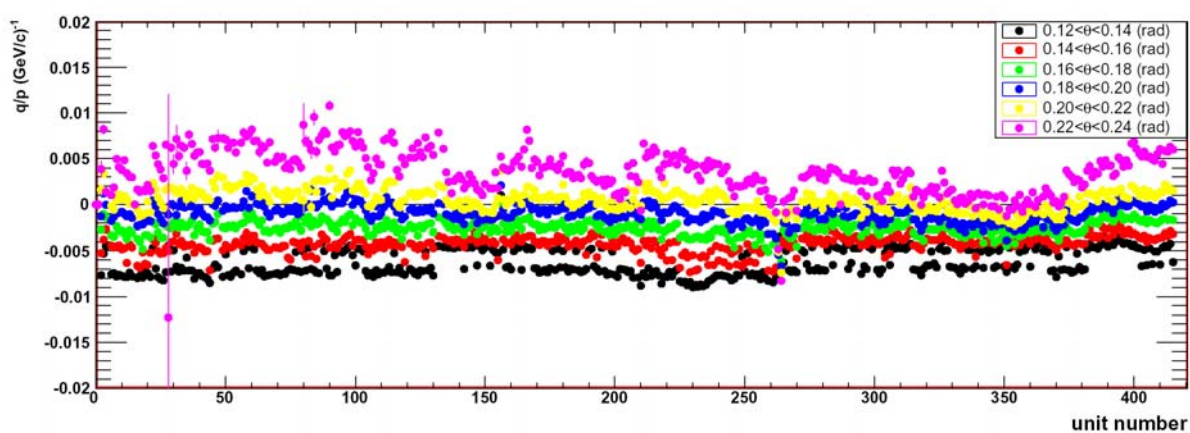


Figure 4.3: The position of the minimum in the raw q/p_{comb} distribution as a function of the unit number for six groups of θ_{TPC} track.

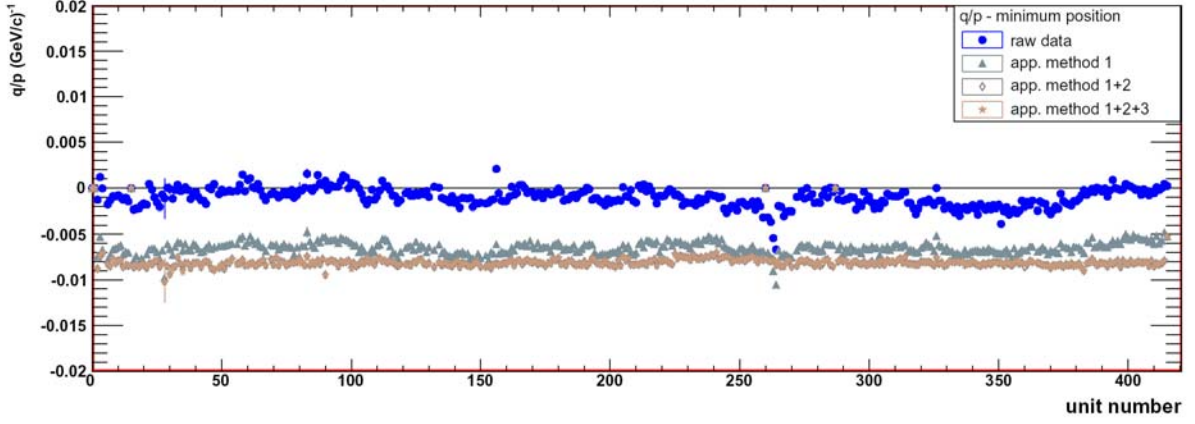


Figure 4.4: Comparison between different methods used to correct the inverse momentum distribution for $\theta \in (0.18, 0.20)$ rad.

$\Delta(1/p_{2,3})(\theta, \phi)$ were extracted from the fit function (Eq. 4.3). Moreover, from $n(q/p, \phi_{TPC})$ histograms, integrated over the ϕ_{TPC} and θ_{TPC} , the minimum position of $\Delta(1/p_2)(unit)$ and $\Delta(1/p_3)(unit)$ for each calibration unit was extracted as well as the average values ($\overline{\Delta(1/p_2)}$, and $\overline{\Delta(1/p_3)}$) for all available statistics were obtained. The combination of these values results in a correction factor given by

$$\Delta(1/p_n)_{method1} = \Delta(1/p_n)(0) \cdot B + \left[\Delta(1/p_n)(\theta, \phi) - \overline{\Delta(1/p_n)} + \Delta(1/p_n)(unit) \right], \quad (4.4)$$

where $n=2,3$ corresponds to the two- or three-parameters fit method, $\Delta(1/p_n)(0)$ is a shift obtained from Monte Carlo simulations and B is a sign of the applied magnetic field in the TPC. In Fig. 4.4 the results of the correction (full triangle) together with the uncorrected data (full circle) are shown. Subsequently, the last two corrections were performed on the pion subsamples identified via an energy loss vs. momentum in the TPC. This allows to increase significantly statistics, but to diminish the purity of the pions samples. Number of pions selected in this manner allows to study the q/p minimum position as a function of θ_{TPC} integrated over an azimuthal angle for each calibration unit separately. Obtained correction factors are given by

$$\Delta(1/p_n)_{method2} = B \cdot \left[\Delta(1/p_n)(\theta, unit) - \overline{\Delta(1/p_n)(\theta, unit)} \right], \quad (4.5)$$

where $\overline{\Delta(1/p_n)(\theta, unit)}$ is the average value integrated over the calibration units and the θ angles. The latter were combined with the one calculated from the so-called “method 1” ($\Delta(1/p_n)_{method1}$) and subtracted from the measured inverse momentum of the track (see Fig. 4.4 (open diamond)). Finally, a last correction is determined in even finer entities of 10 bursts, but integrated over ϕ and θ , so-called “method 3”. The corrected values of the inverse momentum can be expressed as follow

$$(q/p_n)_{corr} = (q/p_n) - \{ \Delta(1/p_n)_{method1} + \Delta(1/p_n)_{method2} + \Delta(1/p_n)(10\ burst) - B \cdot \overline{\Delta(1/p_n)(10\ burst)} \}. \quad (4.6)$$

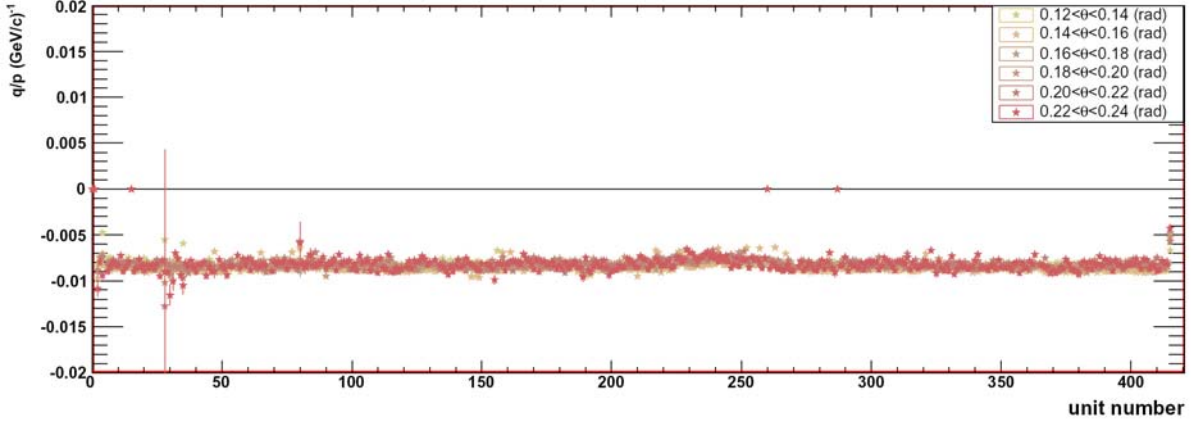


Figure 4.5: Results of the momentum calibration methods. The minimum position of the inverse momentum distribution as a function of unit number for six groups of θ_{TPC} track.

The minimum positions of the fully calibrated q/p distributions as a function of the unit number are shown in Fig. 4.5.

4.5 Energy Loss Calibration

The energy loss of charged particles in the medium occurs mainly via ionization. The mean rate of the energy loss is well described in terms of the Bethe-Bloch equation [WW02] which can be parameterized by

$$\frac{dE}{dx} \approx \frac{A}{\beta^2} \cdot \left(B + C \cdot \ln(\beta^2 \gamma^2) - D \cdot \beta^2 - \frac{\delta}{2} \right), \quad (4.7)$$

in case of the CERES TPC data. The $A - D$ parameters were found based on the analysis of the clear sample of electrons and pions identified through the RICH detectors ($A=13.2$, $B=15.05$, $C=1.08$, $D=4.0$). The last term in the Eq. 4.7 corresponds to the density effect. The latter reduces the relativistic rise from $\sim \ln \gamma^2$ to $\sim \ln \gamma$ at high γ and can be parameterized by [SP71]

$$\begin{aligned} \frac{\delta}{2} &= 4.606 \cdot X + C + a \cdot (X_1 - X)^m & (X_0 < X < X_1), \\ \frac{\delta}{2} &= 4.606 \cdot X + C & (X > X_1). \end{aligned} \quad (4.8)$$

In these formulas δ is expressed as a function of X , defined by $X = \log_{10}(\beta\gamma)$, where the term $4.606 \cdot X$ is simply $2 \ln(\beta\gamma)$. The parameters X_0 and X_1 are particular values of X , such that

$\delta=0$ for $X < X_0$ and for $X > X_1$ δ reaches its asymptotic form. All parameters in Eqs. 4.8 depend on the medium and can be found in literature. For particular composition of the CERES TPC gas mixture the density effect parameters were set to $C = -11.73$, $a = 0.31$, $m = 2.96$, $X_0 = 2.11$, and $X_1 = 4.0$. Since the dE/dx distribution has a long Landau tail, it is common to use in an experiment a truncated mean to characterize the energy loss of a particle. The CERES TPC provided up to 20 samples per measured track (see Section 2.4). The distribution of the truncated mean energy loss as a function of the particles momentum is shown in Fig. 4.6. The contours depicted in Fig. 4.6 follow the parameterization explained above and are used to select protons and pions for two particle correlation analysis presented in the following chapters. The TPC dE/dx resolution depends on the number of hits; the average resolution is 10 % [Yur06]. In addition to the unit-by-unit calibration of dE/dx accomplished during the data production, a finer granulated calibration was performed on the output of the `step3c`. Monitoring of the dE/dx pion peak position for a given range of the particle momentum was performed for every 10 bursts. The correction factor chosen such as to bring the mean dE/dx of pions to its nominal value, was applied to each measurement within the 10 bursts. As the fluctuations of the dE/dx pion peak position as a function of time are rather small the influence of this calibration on the

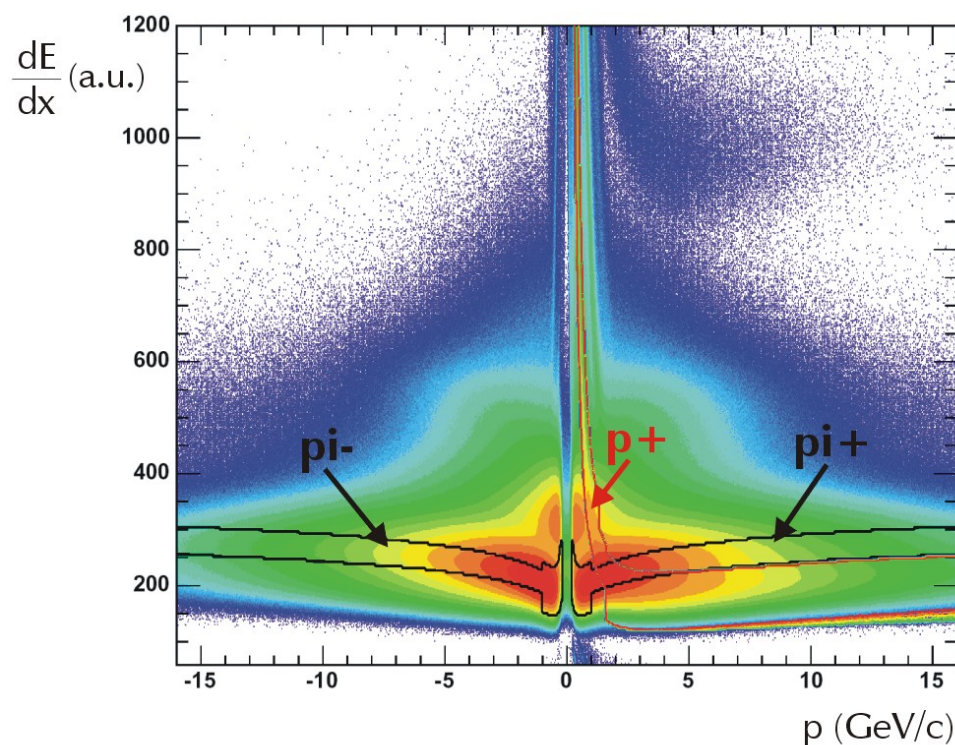


Figure 4.6: The energy loss as a function of particle momentum from the TPC tracks. The contours represent the pion and proton cuts used in the correlation analysis.

obtained resolution is not very significant.

4.6 Matching Calibration

In the CERES experiment the position of particles was measured mainly by the SDD and the TPC. Each of these subdetectors reconstructed tracks from hits induced by particles moving through its active volume. Therefore, in order to obtain complete paths of particles created during the collision, tracks from the SDD and the TPC were combined to TCP-SDD tracks based on the calculation of the opening angles ($\Delta\theta$, $\Delta\phi$). The latter was calculated for each combination of tracks recorded by subdetectors, and a pair with the minimum opening angle was chosen as the best candidate for the TCP-SDD track. In order to account for the geometrical effects in the subdetectors and the different track reconstruction efficiency the matching distribution $n(\Delta\theta, \Delta\phi)$ was calculated for each unit separately in bins of

- inverse momentum (7),
- azimuthal angle (48),
- polar angle (7),
- numbers of anodes per reconstructed hit in SDD (2).

The hit resolution of the SDD depends on the number of anodes on which the induced signal was recorded. Thus, the first of the bin represents the SDD tracks which were reconstructed from the multi-anode hits in both silicon detectors only, and the second bin describes the rest. The obtained distributions were projected on $\Delta\theta$ and $\Delta\phi$ axis, respectively, and fitted by one-dimensional Gaussian to extract the mean position of the peak. The correction factors, derived for each unit, represent a deviation of the mean positions of the matching distribution from zero. In Fig. 4.7 an example of two-dimensional distribution of the opening angle (top left panel) together with the projections on $\Delta\phi$ (bottom left panel) and $\Delta\theta$ (bottom right panel) axis, for a sample of reconstructed track with inverse momenta $-0.7 < 1/p < -0.4$ (GeV/c)⁻¹, polar angle between 0.16 and 0.18 radians, and azimuthal angle from -0.52 to -0.39 radians, are shown. The influence of the uncorrelated matching between TPC and SDD tracks on the extracted mean position was studied by subtracting background distribution from the signal distribution. The background matching distribution was obtained by choosing the TPC and SDD track from different events and finding the best candidate for the TPC-SDD track, similar as for tracks originating from the same event. An example of the derived background distributions (blue histogram) normalized to the tails of the signal distributions (green histogram) is shown in the two bottom panels in Fig. 4.7. The mean position of the background-free matching distribution does not differ significantly from the raw matching distribution, therefore, the background subtraction was neglected in this calibration step. In addition to the unit-by-unit calibration, the

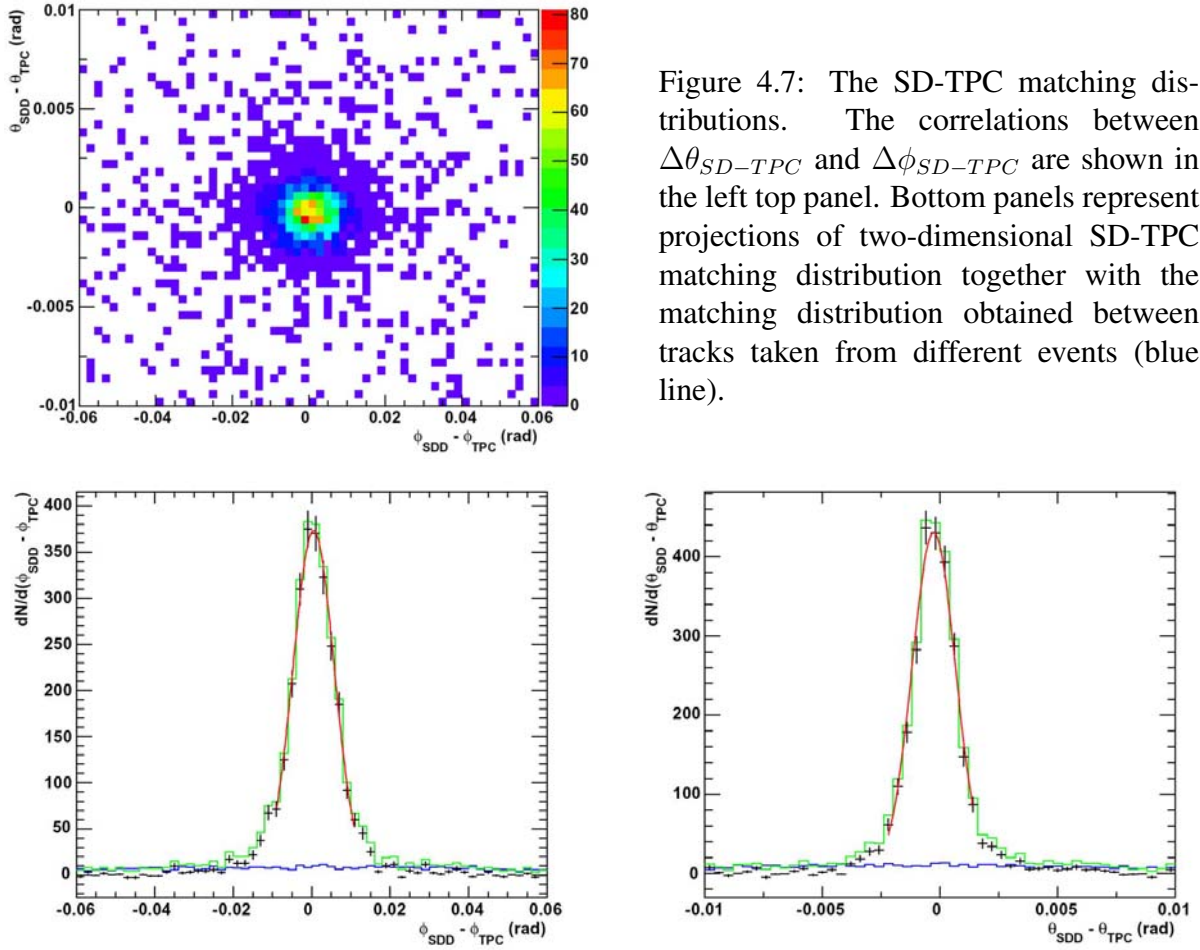


Figure 4.7: The SD-TPC matching distributions. The correlations between $\Delta\theta_{SD-TPC}$ and $\Delta\phi_{SD-TPC}$ are shown in the left top panel. Bottom panels represent projections of two-dimensional SD-TPC matching distribution together with the matching distribution obtained between tracks taken from different events (blue line).

matching distributions were corrected for the deviations in the azimuthal direction originating from the presumably time-independent imperfections in the chamber alignment, dead electronics channels, etc. In Fig. 4.8 example distributions of the $\Delta\phi$ (left panel) and the $\Delta\theta$ (right panel) as a function of the azimuthal angle of the TPC track are shown. The mean position for each ϕ_{TPC} slice was derived by fitting with a Gaussian. The correction was performed in the 7 bins of the polar angle and in two classes of the anode number per hit recorded in the SDD. The narrow bins allow to solve the fine structures of the distortions in the azimuthal angle. The data set was integrated over the positive and negative magnetic field units. Two calibration maps were obtained to recenter the $\Delta\phi$ and the $\Delta\theta$ at zero for given ϕ value.

The quality of the TCP-SDD tracks directly depends on the spatial resolution of the detectors and on the multiple scattering in the material. For tracks with high enough momentum the matching quality depends only on the spatial resolution, whereas, for the low momentum tracks the matching quality is deteriorated due to the multiple Coulomb scattering in the detector ma-

terial. The multiple Coulomb scattering is approximated by the deflection angle [LD91, E⁺04]

$$\Theta_0 = \frac{13.6 \text{ MeV}}{\beta c p} \approx \sqrt{\frac{L}{X_0}} \left\{ 1 + 0.038 \ln \left(\frac{L}{X_0} \right) \right\} \quad (4.9)$$

where X_0 is the radiation length of the medium, L is the thickness of the medium, p , $c\beta$, and z are the momentum, the velocity, and the charge of the incident particle, respectively. The matching quality is reflected in the width of the opening angle distributions ($\Delta\theta$, $\Delta\phi$), which has been studied under the different conditions (p , θ_{TPC} , number of anodes per hit in the SDD). The width of the matching distribution was parameterized as a function of the inverse momentum ($1/p$) by

$$\Delta\theta = \sqrt{P0_{\Delta\theta}^2 + \left(\frac{P1_{\Delta\theta}}{p} \right)^2} \quad (4.10)$$

where $P0_{\Delta\theta}$ corresponds to the angular detector resolution, and $P1_{\Delta\theta}$ stands for the contribution from the multiple Coulomb scattering. For the $\Delta\phi$ distributions a similar parameterization was performed. After implementing the corrections explained above the $n(\Delta\theta, \Delta\phi)$ distributions integrated over azimuthal angle and the data units were produced for bins of the track θ angle and the inverse momentum. The background distributions were subtracted from the signal distributions. The $\Delta\theta$ and the $\Delta\phi$ projections were fitted with a Gaussian in order to extract the width and the mean position for each the θ angle and the inverse momentum bin. The derived widths were plotted as function of the inverse momentum and fitted for each θ slice by the Eq. 4.10. The fit coefficients obtained for three classes of the SDD hit configurations (Fig. 4.9) were parameterized by

$$P_n(\theta_{TPC}) = \frac{1}{A + B \cdot \theta_{TPC} + C \cdot \theta_{TPC}^2 + D \cdot \theta_{TPC}^4 + E \cdot \theta_{TPC}^6}. \quad (4.11)$$

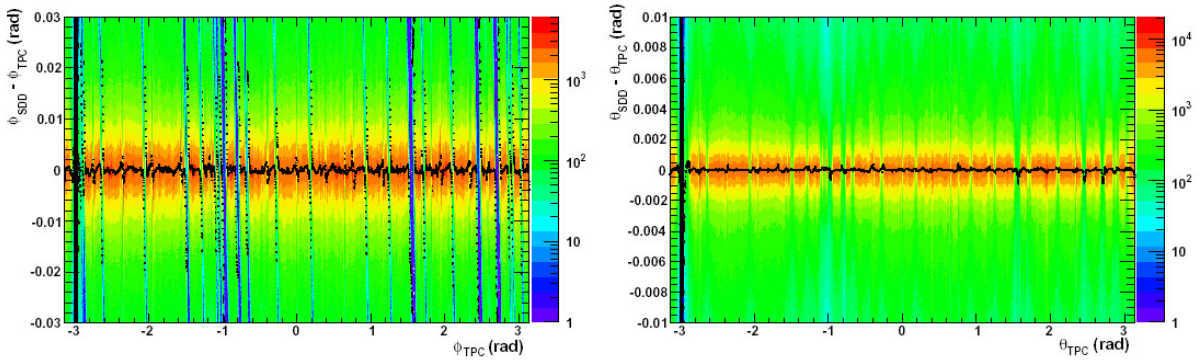


Figure 4.8: The difference between the SDD and TPC angles vs. ϕ TPC track angle (left plot for ϕ , and right plot for θ). The black points represent the mean position obtained by fitting Gauss distribution to each ϕ_{TPC} slices.

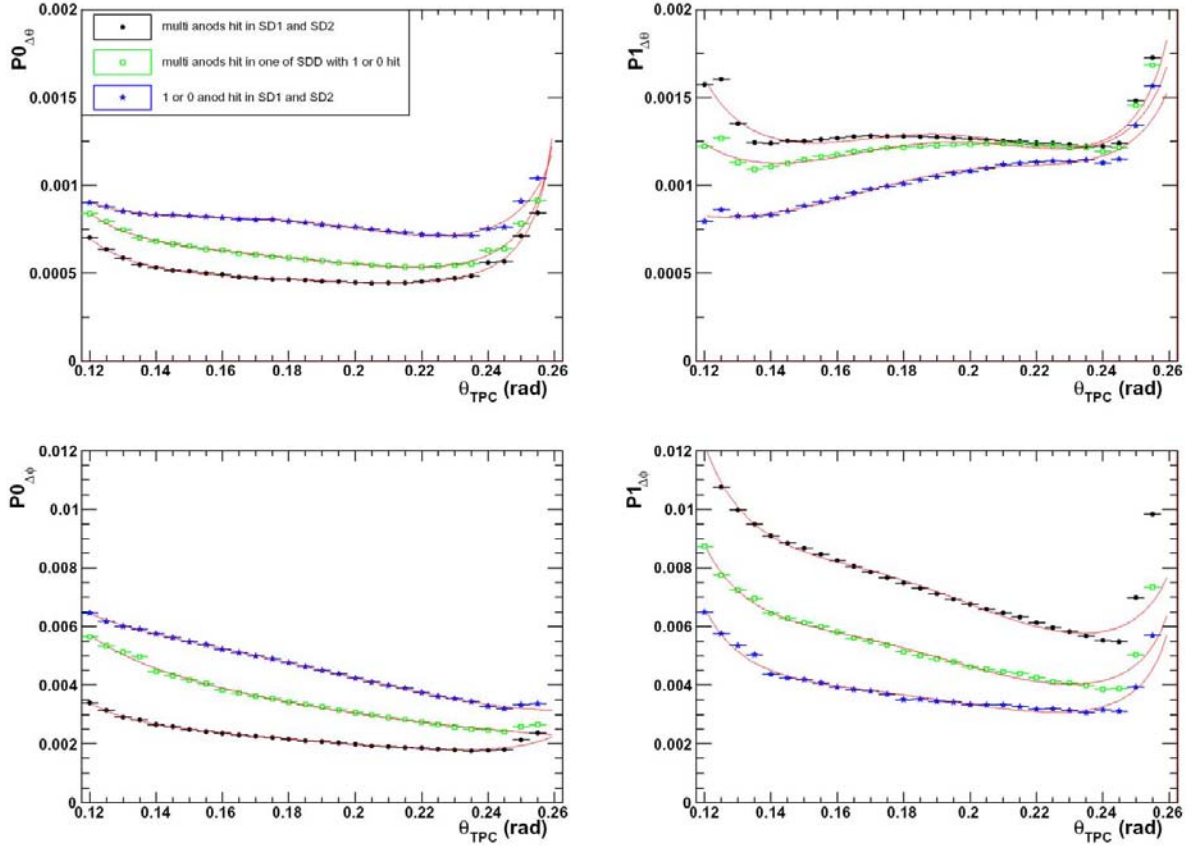


Figure 4.9: The obtained parameters $P0$ and $P1$ describing the momentum dependence of the width of the TPC-SD matching distributions, plotted as a function of θ .

4.7 Reaction Plane Calibration

The distance between the trajectories of two colliding nuclei is called the impact parameter $|\vec{b}|$ and is an important parameter of a nucleus-nucleus collisions. Fig. 4.10 depicts schematically a collision of two nuclei in the center-of-mass system. Using information about the impact parameter and defining the beam axis to be the z axis, the reaction (event) plane is characterized by the angle Ψ_n between the \vec{b} and the x axis. In the limit of central collisions, $|\vec{b}| \rightarrow 0$, the reaction plane cannot be defined.

4.7.1 Determination of the Event Plane

The information about the impact parameter \vec{b} in experiments can be accessed only indirectly (see Section 4.8). The orientation of the reaction plane can be reconstructed from the collision

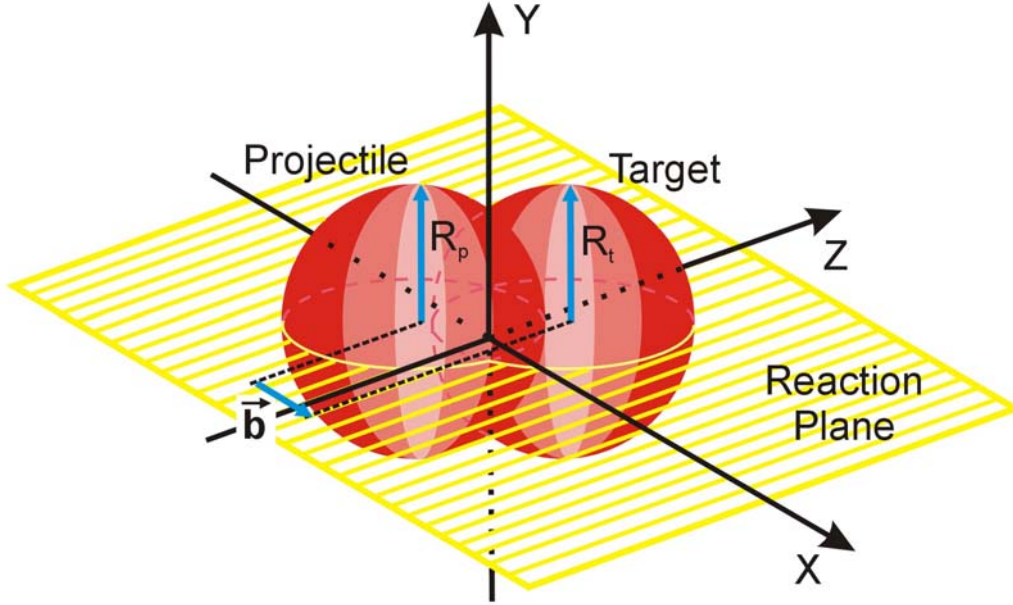


Figure 4.10: Schematic view of a semi-central collision in the center-of-mass frame. The reaction plane is defined by the impact parameter b and the z (beam) axis. The R_p and R_t corresponds to the radius of the projectile and the target nucleus, respectively.

products. In the CERES experiment, the reaction plane is reconstructed based on the azimuthal distribution of charged particles emitted around midrapidity [Oll95, VZ96]. The method uses the anisotropic flow itself to determine the event plane which means that the event plane can be determined independently for each harmonic (n) of the anisotropic flow. For each event the reaction plane vector \vec{Q}_n is defined by the equation:

$$\vec{Q}_n = (Q_n^X, Q_n^Y) = \frac{1}{N} \sum_{i=1}^N w_i \exp(in\phi_i) \quad (4.12)$$

where N is the total particle multiplicity and ϕ_i is the azimuthal angle of the i -th particle. The weights w_i are chosen to optimize the reaction plane resolution. Usually the weights for the odd and even harmonic planes are different. One can weight each particle with its rapidity in case of the first harmonic or with the transverse momentum in case of the second harmonic, as it was done in the presented analysis. In Fig. 4.11 an example two-dimensional distribution of the reaction plane vector \vec{Q}_2 is shown. For a given n -th harmonic, the orientation of the reaction plane can be derived from the relation

$$\Psi_n = \frac{1}{n} \arctan\left(\frac{Q_n^Y}{Q_n^X}\right). \quad (4.13)$$

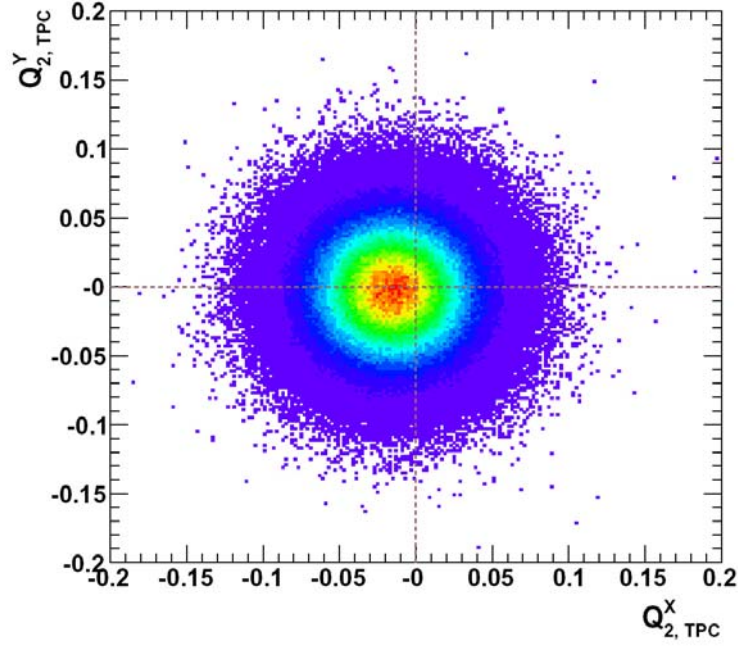


Figure 4.11: The raw $Q_{2,TPC}^Y$ vs. $Q_{2,TPC}^X$ distribution obtained from the TPC tracks.

In order to suppress fake tracks and decay products of long lived resonances in the calculation of the Q_n^X and Q_n^Y the matching between TPC and SDD was required to be better than 5σ . Furthermore, the following quality cuts were applied for each track

- $0.125 \leq \theta_{TPC} \leq 0.235$ (fiducial acceptance)
- $\chi_{phi}^2 \leq 4.0$ and $\chi_{rad}^2 \leq 3.0$ (χ^2 of the track fit)
- $N_{FH} \geq 10$ (number of fitted hits on the TPC track)
- $0.025 \text{ GeV}/c \leq p_{\perp} \leq 4.0 \text{ GeV}/c$ (p_{\perp} range).

The reaction plane angle Ψ_n determined from the n -th harmonic is in the range between $-\pi/n$ and π/n . For analysis of the HBT radii dependence on the reaction plane orientation presented in this work the second Fourier coefficients derived from the TPC tracks were used to calculate the event plane.

4.7.2 Acceptance Corrections

The distribution of the azimuthal angle of the reaction plane, $dN/d\Psi_n$, is isotropic since the orientation of the impact parameter is random in the collision of heavy-ions. The reaction

plane distribution measured in the experiment, on the other hand, is not always uniform (see Fig.4.12). The particle distribution becomes azimuthally anisotropic mostly due to the finite acceptance of the detector and fluctuation of the beam position in respect to the experimental setup. Before the information about the reaction plane orientation can be further used, methods to remove the effects of anisotropy have to be applied. In the simplest approach, the distribution of (Q_n^X, Q_n^Y) is recentered [B⁺97] by subtracting the $(\langle Q_n^X \rangle, \langle Q_n^Y \rangle)$ values previously averaged over groups of events (for each unit such corrections were found). This method allows to remove effectively the first harmonic from the distribution of Ψ_n . In Fig. 4.13, the two plots represent the correction factor $(\langle Q_n^X \rangle, \langle Q_n^Y \rangle)$ obtained for the particle track recorded by the TPC. The two plots in Fig. 4.14 show the result of the recentering method. After applying this correction, the raw distribution of the reaction plane angle becomes as shown in the middle panel of Fig. 4.12. Further correction has to be applied to remove the remaining anisotropy. The next step uses the width of the (Q_n^X, Q_n^Y) distribution to remove the second harmonic from the distribution of Ψ_n . The Q_n^X and Q_n^Y widths as a function of the unit number are shown in Fig. 4.15. With both corrections, the components (Q_n^X, Q_n^Y) of the reaction plane vector \vec{Q}_n become

$$\begin{aligned} Q_{n,cor}^X &= \frac{Q_n^X - \langle Q_n^X \rangle}{\sigma(Q_n^X)}, \\ Q_{n,cor}^Y &= \frac{Q_n^Y - \langle Q_n^Y \rangle}{\sigma(Q_n^Y)}. \end{aligned} \quad (4.14)$$

The reaction plane orientation angle, Ψ_n , is then calculated from equation 4.13 using $Q_{n,cor}^X$ and $Q_{n,cor}^Y$. Its distribution is reasonably flat (Fig. 4.12, right panel).

4.7.3 Reaction Plane Resolution

In the experiment, the reconstructed reaction plane angle, Ψ_n , differs in general from the true reaction plane orientation Ψ by a finite angle $\Delta\Psi = \Psi_n - \Psi$. This is caused by the finite number of detected particles, detector coverage and resolution, and finite-number fluctuations. Quantitatively, the knowledge about these differences is of great importance for analysis of the azimuthal anisotropy like the flow or the HBT vs. reaction plane. Different methods were proposed to account for this effect in measured observables [OI197, PV98]. Expressing azimuthal distribution as Fourier series (see Eq. 1.20) and averaging over many events, assuming that Ψ and $\Delta\Psi$ are statistically independent, it is possible to obtain a relation between the reconstructed and true Fourier coefficients

$$\langle \cos(n\Psi_n) \rangle = \langle \cos(n\Psi) \rangle \langle \cos(n\Delta\Psi) \rangle. \quad (4.15)$$

The resolution of the reconstructed reaction plane is often expressed in terms of a correction factor $\cos(n\Delta\Psi)$. Following [OI197] the distribution of the azimuthal angle deviation $\Delta\Psi$ can

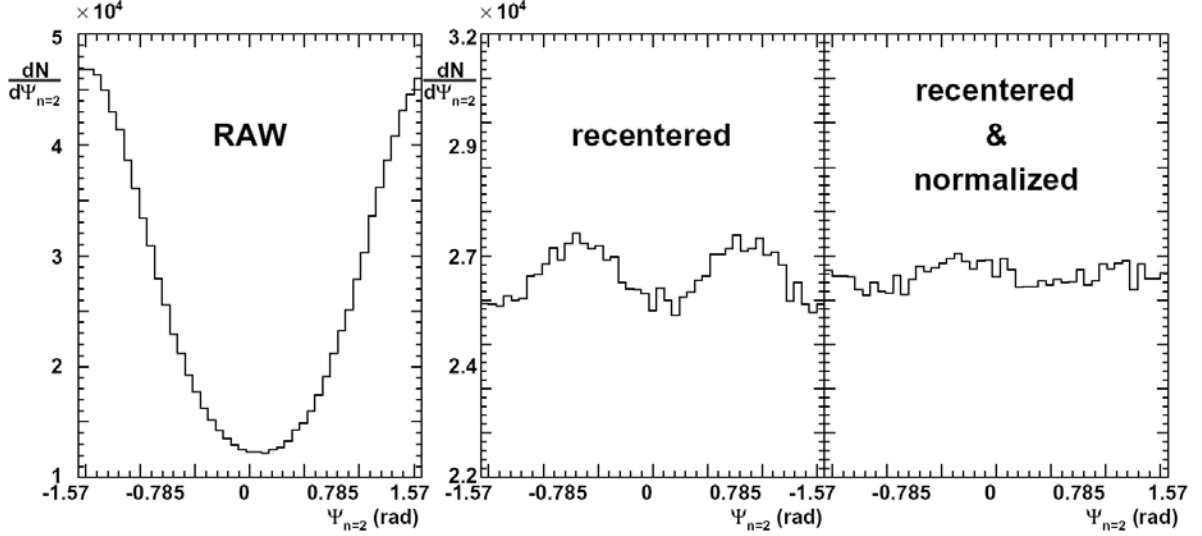


Figure 4.12: The distribution of the reaction plane angle Ψ_2 : raw experimental data – tracks recorded by TPC (RAW), after applying the recentering method, and after dividing the Q components by the widths of the (Q_n^X, Q_n^Y) distribution.

be expressed in terms of a real parameter χ , which measures the accuracy of the reaction plane determination

$$\frac{dN}{d\Delta\Psi} = \frac{1}{\pi} \exp(-\chi^2) \left\{ 1 + z\sqrt{\pi} [1 + \text{erf}(z)] \exp(z^2) \right\} \quad (4.16)$$

where $z = \chi \cos(\Delta\Psi)$ and $\text{erf}(z)$ is the error function. The Fourier coefficients can be obtained by integrating Eq. 6 in [Oll97] first over $\Delta\Psi$ and then over Q

$$\langle \cos(n\Delta\Psi) \rangle = \frac{\sqrt{\pi}}{2} \chi \exp(-\chi^2/2) \left[I_{\frac{n-1}{2}} \left(\frac{\chi^2}{2} \right) + I_{\frac{n+1}{2}} \left(\frac{\chi^2}{2} \right) \right] \quad (4.17)$$

where I_k is the modified Bessel function of order k . The parameter χ can be derived by dividing randomly each event into two (or more) subevents. Consequently, for those subevents the reaction plane angles Ψ_n are reconstructed resulting in $\Psi_{n,SE1}$ and $\Psi_{n,SE2}$. However, since each subevent contains only $N/2$ particles, corresponding χ parameter scales as $\chi_{SE1} = \chi_{SE2} = \chi/\sqrt{2}$. The distribution of the relative angle $\Delta\Psi_R \equiv |\Psi_{SE2} - \Psi_{SE1}|$ can be calculated analytically

$$\frac{dN}{d\Delta\Psi_R} = \frac{\exp(-\chi_{SE1}^2)}{2} \left\{ \frac{2}{\pi} (1 + \chi_{SE1}^2) + z [I_0(z) + L_0(z)] + \chi_{SE1}^2 [I_1(z) + L_1(z)] \right\} \quad (4.18)$$

where $z = \chi_{SE1}^2 \cos(\Delta\Psi_R)$, and L_0, L_1 corresponds to modified Struve functions. The value of χ can be obtained by fitting Eq. 4.18 to the measured distribution of $\Delta\Psi_R$. Therefore,

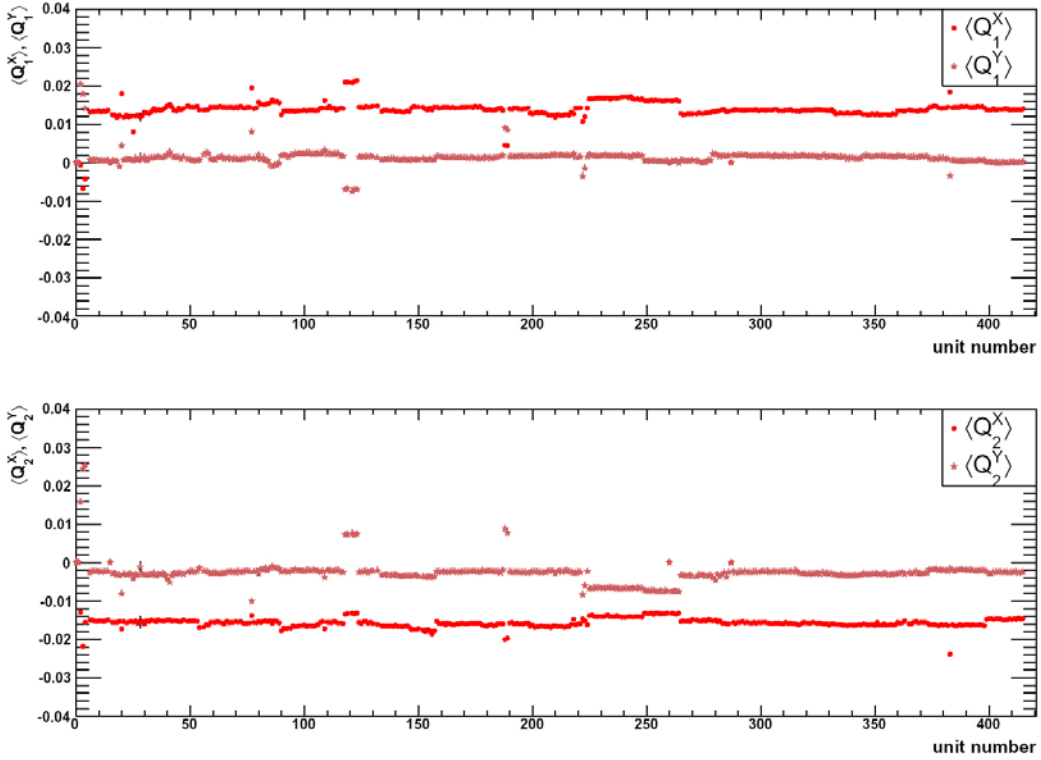


Figure 4.13: The average value of (Q_n^X, Q_n^Y) obtained for a given unit number, raw data (first and second harmonic).

the reaction plane resolution can be expressed in terms of $\langle \cos(n\Delta\Psi) \rangle$ by solving Eq. 4.17. Alternatively, one can obtain the correction factor $\langle \cos(n\Delta\Psi) \rangle$ from the relation [PV98]

$$\langle \cos(n\Delta\Psi) \rangle = \sqrt{2} \langle \cos[n(\Psi_{SE1} - \Psi)] \rangle \quad (4.19)$$

where

$$\langle \cos[n(\Psi_{SE1} - \Psi)] \rangle = \sqrt{\langle \cos[n(\Psi_{SE2} - \Psi_{SE1})] \rangle}. \quad (4.20)$$

The estimation of the reaction plane resolution in CERES experiment was based on both presented method. The particle tracks per each event, recorded by SDD or TPC, were divided into two subsets $SE1$ and $SE2$. For each subset the reaction plane orientation was calculated and the difference $\Psi_{n,SE2} - \Psi_{n,SE1}$ was derived. The obtained difference was accumulated over many events and stored in centrality classes. The reaction plane resolution as a function of the collision centrality is shown in Fig. 4.16.

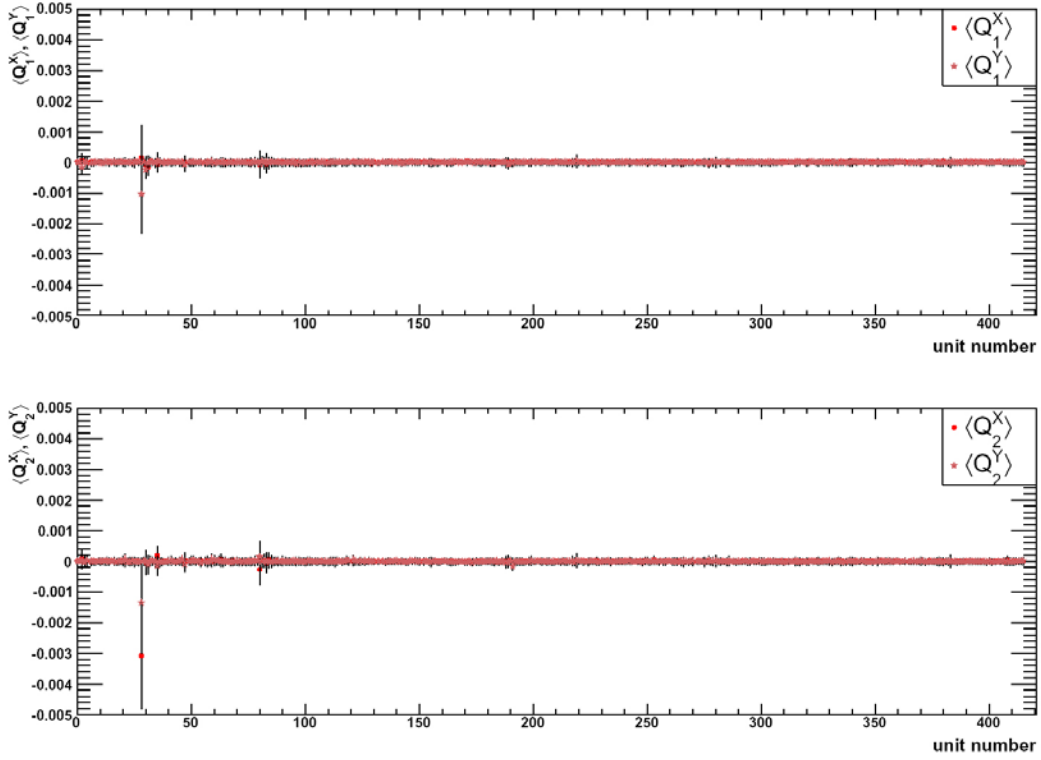


Figure 4.14: The recentered average value of (Q_n^X, Q_n^Y) as a function of unit number.

4.8 Centrality Determination

The nuclear overlap model [EKL89] represents a nucleus-nucleus collision in terms of binary collisions between nucleons. Based on the density distributions within the two colliding nuclei, the number of participating nucleons and of binary NN collisions are expressed as functions of the impact parameter $\vec{b} \equiv \langle \vec{r}_B \rangle - \langle \vec{r}_A \rangle$, and the total geometric cross section is calculated. The nuclear density $n_A(r)$ distribution, defined as the number of nucleons per unit volume, can be approximated by a Woods-Saxon profile

$$n_A(r) = \frac{n_0}{1 + \exp\left(\frac{r-R}{d}\right)}, \quad (4.21)$$

where $n_0 = 0.17 \text{ fm}^{-3}$ is a density of nucleons at the center, $R = (1.12A^{1/3} - 0.86A^{-1/3}) \text{ fm}$ is the half-density radius, and d the surface thickness chosen to be 0.54 fm. The $n_A(r)$ is normalized to the number of nucleons

$$\int d^3r n_A(r) = 4\pi \int_0^\infty r^2 dr n_A(r) = A. \quad (4.22)$$

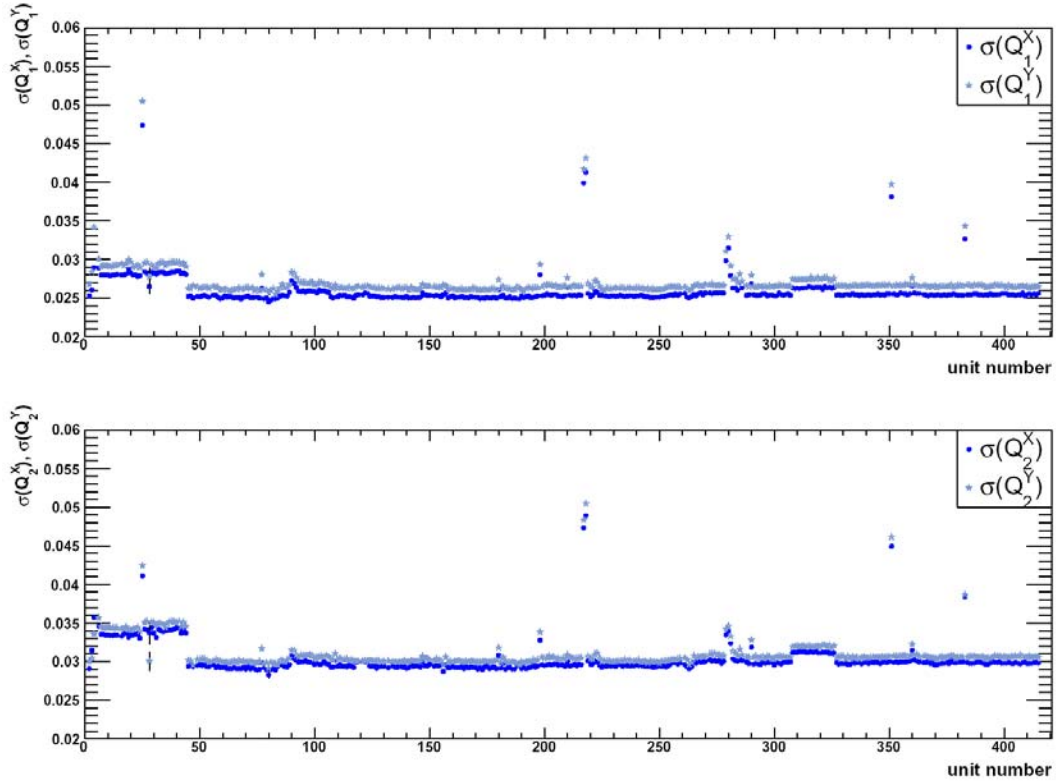


Figure 4.15: The width of the Q_n^X and Q_n^Y distribution as a function of the unit number.

For the following consideration it is convenient to introduce the nuclear thickness function defined as the density distribution integrated along the beam axis z

$$T_A(b) = \int_{-\infty}^{\infty} dz n_A(\sqrt{b^2 + z^2}), \quad (4.23)$$

also normalized to A

$$\int d^2b T_A(b) = A. \quad (4.24)$$

For a given \vec{b} , the overlap function is defined as the product of the thickness functions of the colliding nuclei A and B, integrated over the two transverse dimensions

$$T_{AB}(b) = \int d^2s T_A(\vec{s}) T_B(\vec{s} - \vec{b}), \quad (4.25)$$

where \vec{s} and \vec{b} are perpendicular to the beam direction. The normalization condition for the thickness function is given by

$$\int d^2b T_{AB}(b) = AB. \quad (4.26)$$

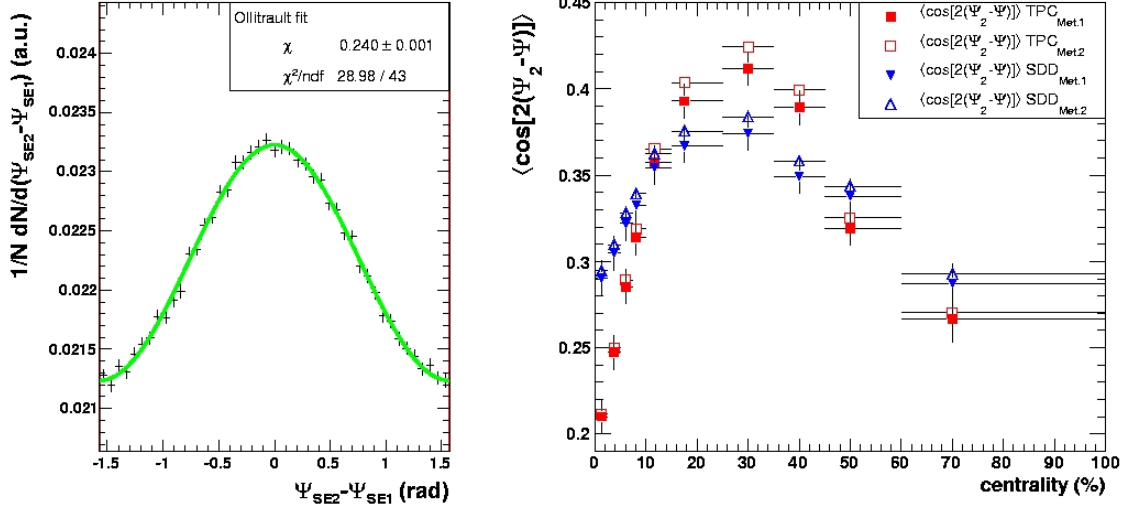


Figure 4.16: Left panel: difference between the reaction plane orientation from two sub-events for the most central data bin. The solid line (green) is the Ollitrault fit to the distribution. Right panel: the $\langle \cos[2(\Psi_2 - \Psi)] \rangle$ obtained from the two different methods is shown as a function of centrality. The resolution of the reaction plane orientation calculated from TPC tracks and from SDD tracks is shown as squares and triangles, respectively. The full symbols correspond to the method proposed in [Oll97] (Met.1), and the open symbols were obtained for the method proposed in [PV98] (Met.2).

The product $T_{AB}(b) \cdot \sigma_{NN}$ can be interpreted as the number of binary NN collisions in A+B collision at given \vec{b} , with σ_{NN} being the total inelastic nucleon-nucleon cross section: $N_{AB}^{coll}(b) = T_{AB}(b) \sigma_{NN}$.

Defining “participants” as the nucleons which have encountered at least one binary collision it is possible to calculate the mean number of participants of an A+B collisions at a given impact parameter via

$$\begin{aligned}
 N_{AB}^{part}(b) = & \int d^2s T_A(\vec{s}) \left\{ 1 - \left[1 - \frac{\sigma_{NN} T_B(\vec{s} - \vec{b})}{B} \right]^B \right\} \\
 & + \int d^2s T_B(\vec{s}) \left\{ 1 - \left[1 - \frac{\sigma_{NN} T_A(\vec{s} - \vec{b})}{A} \right]^A \right\}. \quad (4.27)
 \end{aligned}$$

The expression in the curly brackets represents a probability of becoming a participant.

The total geometric cross section, σ_{GEOM} , is the cross section for such A+B collisions that at least one binary NN collision occurs. Using a Poisson distribution the σ_{GEOM} can be written

as

$$\sigma_{GEOM} = \int d^2b [1 - \exp(-T_{AB}(b) \sigma_{NN})] . \quad (4.28)$$

The geometrical cross section of Pb+Au at $\sqrt{s_{NN}} = 17.2$ GeV is equal to 6.94 barn (b) derived from the overlap model with a Woods-Saxon nucleus density profile and a binary NN collision cross section of $\sigma_{NN}=30$ mb [Miś04]. Three observables related to the centrality are directly¹ available in the `step3c` output data: the MC amplitude, the track multiplicity in the SDD ($0.10 < \Theta < 0.26$), and the track multiplicity in the TPC ($0.12 < \Theta < 0.24$, $N_H > 13$). In the following, these three variables are called “multiplicities”. The centrality calibration means finding the relation between a multiplicity on one side and the impact parameter, or, equivalent to it but more commonly used, the percentage of geometrical cross section σ_{GEOM} on the other. The calibration was done in two steps, described in Sections 4.8.1. First, a low beam intensity minimum bias run (unit 218, run 1424, bursts 0-201) was used to find the calibration tables for the three multiplicities. The correlations between the three multiplicities in a minimum bias run are presented in Fig. 4.17. Second, the run-by-run variation was checked and factors

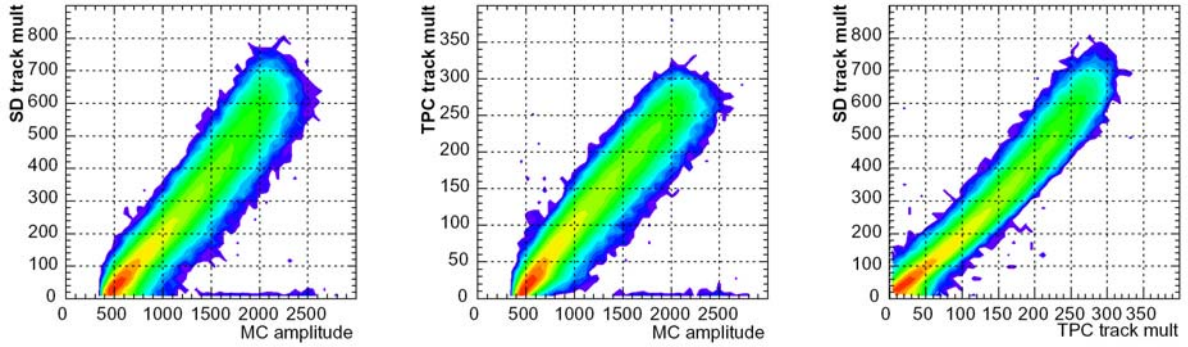


Figure 4.17: Correlations between the three multiplicities in the low intensity minimum bias run.

which allow to scale multiplicities in all runs were found such that the corrected high edge was at the same place as the edge in unit 218. Before performing these two steps, the systematic dependence of the multiplicities on the running conditions was studied. For this, distributions recorded in different runs were normalized to 10^6 incident beam particles. The normalization was performed as follows

$$n_{cent}(m) = \frac{n_{0,cent}(m)}{N_{0,cent}} \cdot \frac{cent}{beam} \cdot 10^6 \quad (4.29)$$

$$n_{minb}(m) = \frac{n_{0,minb}(m)}{N_{0,minb}} \cdot \frac{minb}{beam} \cdot 10^6 \quad (4.30)$$

¹Other variables can be, of course, generated by looping over tracks.

$$n_{beam}(m) = \frac{n_{0,beam}(m)}{N_{0,beam}} \cdot \frac{beam}{beam} \cdot 10^6, \quad (4.31)$$

where $n_0(m)$ and $n(m)$ are the raw and the normalized multiplicity distributions. The *beam*, *minb*, and *cent* are the numbers of beam, minimum bias, and central trigger candidates seen in the scalers (no deadtime); and $N_{0,i}$ is the integral of the $n_{0,i}(m)$ histogram for $i = (beam, minb, cent)$ respectively. This way the DAQ deadtime factor and the losses introduced via event cuts are corrected for, the only assumption being that they do not introduce any centrality bias. The normalized multiplicities obtained with the beam and the minimum bias trigger at low beam intensity together with the data obtained for central and the minimum bias trigger for high intensity beam are shown in Fig. 4.18. The MC amplitude (above ADC pedestal equal to 380) and the TPC multiplicity are roughly proportional. The SDD multiplicity increases with centrality faster than the other two indicating that random hit coincidences are not negligible. Similar increase is visible in Fig. 4.18 (middle panel) for runs taken under the high beam intensity. Moreover, the SDD multiplicity is sensitive to noise as can be seen by the presence of high signals in the run without the target (counting only tracks with a good matching between the two SDD's might give a more reliable track multiplicity). Delta electrons produced by a beam particle passing without a nuclear interaction can be shown by comparing the beam trigger and random pulser trigger events. The bump at TPC multiplicities below 50 might come from interactions in other than gold materials. According to the overlap model the maximum number of participants in Pb+C collision should be 7-8 times lower than in Pb+Au collision at the top SPS energy. This is consistent with the position of the upper edge of the bump.

4.8.1 Centrality Calibration

The minimum bias run 1424 was particularly clean since it was taken with a reduced beam intensity. The number of events n per beam particle can be transformed to cross section σ by multiplying it with 521 barn

$$\sigma = n \cdot \frac{m_{Au}^{mol}}{N_A \rho d} = n \cdot \frac{196.967 \text{ g}}{6.022 \cdot 10^{23} \cdot 19.32 \text{ g/cm}^3 \cdot 325 \mu\text{m}} = n \cdot 521 \text{ b} \quad (4.32)$$

where m_{Au}^{mol} is a molar mass of gold, N_A is the Avogadro number, and ρ and d are the density of gold at 293 K and the thickness of the target ($13.25 \mu\text{m}$), respectively. The normalized distributions from the low intensity minimum bias run, shown in the previous section, are thus multiplied by $521/10^6$ and subsequently integrated from right to left. The integral has the meaning of the cross section for events with the multiplicity above a given value. In Fig. 4.19 the normalized multiplicity distribution together with the ratio of the integrated cross section to the geometrical cross section is shown. The centrality as a function of multiplicities, obtained in this fashion, was saved on ASCII files and used to convert the measured multiplicity to the percentage of the geometrical cross section σ_{GEOM} . Integrating the entire multiplicity range

triggered on in the central run 1427 gives 7.35 %. The events with centralities above the 45 % σ_{GEOM} are contaminated by non-target interactions.

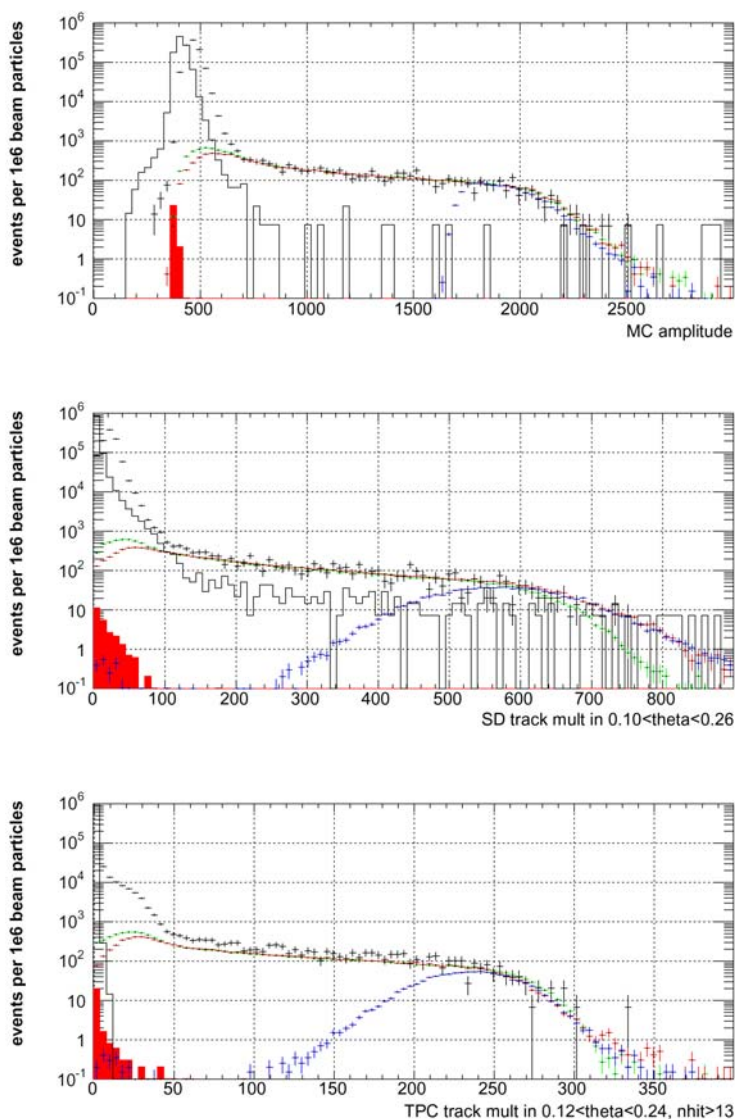


Figure 4.18: Multiplicity distributions taken under different running conditions: beam (black) and minimum bias (green) triggers at low beam intensity (runs 1423 and 1424); minimum bias (red) and central (blue) events at high beam intensity (runs 1420 and 1427). The full red histogram represents events taken with the MT (random pulser) trigger during minimum bias run 1424. The solid black histogram represents run 1244: no target, beam trigger, high beam intensity.

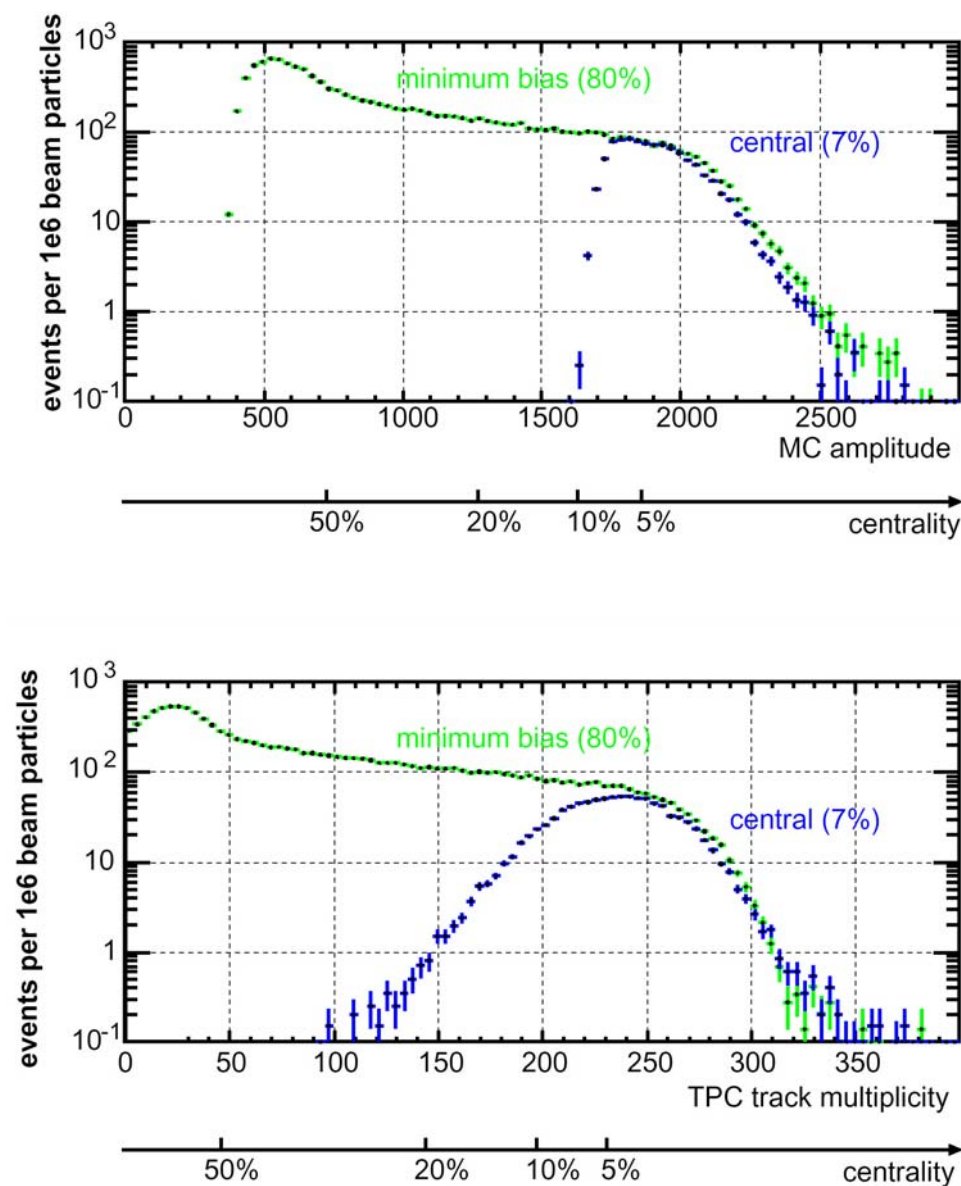


Figure 4.19: Multiplicity distributions from the minimum bias run at low beam intensity (green), normalized to 10^6 beam particles. For comparison, a central run taken at high beam intensity is shown as well (blue).

The position of the upper edge of the multiplicity distributions can vary run-by-run due to various technical reasons. In order to monitor these variations and to correct for them, the edge position was determined in each unit. This was done in two independent ways:

- by finding such multiplicity value that the number of events with a multiplicity equal or higher than it corresponds to 200 mb,
- by fitting the

$$f(m) = \frac{A}{1 + \exp\left(\frac{m - E_{pos}}{C}\right)} \quad (4.33)$$

to the multiplicity distribution, and extracting the E_{pos} parameter.

The results of these two methods of the edge determination are shown in Fig. 4.20 as blue and black points, respectively. The run-by-run variations were 6 % for MC, 5 % for SD, and 9 % for TPC (peak-to-peak). The green plot represents the blue to black ratio; both methods agree within 4 %. Since the fit method seems more reliable and does not seem to introduce any systematic difference between the minimum bias and central runs it was chosen for the centrality calibration for data collected during 2000 run. The distributions of calibrated centrality for the events used for the two particle correlation analysis are shown in the Fig. 4.21. The data were taken with three different triggers. This is best reflected in the centrality distribution recorded by Multiplicity Counter, used for triggering during the run 2000. Ideally the centrality distribution recorded by TPC should follow the MC. The width of the SD and TPC edges can be used as the upper limit on the respective centrality resolutions. The impact parameter b can be calculated from centrality fraction c using the relation

$$\pi b^2 = c \cdot 6.94 \text{ b.} \quad (4.34)$$

4.9 Charged Particle Multiplicity

As described in the previous subsection, the number of detected particle tracks varies with the impact parameter. The absolute multiplicity of charged particles N_{ch} can be determined for events within a reasonably narrow bin of centrality. The minimum bias data (100 bursts of run 1424 from `step2`) recorded during the 2000 run were chosen for this analysis. Out of the two high resolution tracking detectors of CERES, SDD and TPC, the first one is more suitable for this kind of analysis because it allows to select the vertex tracks. In order to minimize an inefficiency of the detector the analysis was restricted to a ϕ -range within

- SDD1 covered $-1.81 < \phi < -1.61$ and $0.40 < \phi < 0.60$ radian,
- SDD2 covered $-1.83 < \phi < -1.58$ and $0.38 < \phi < 0.62$ radian,

where all anodes worked properly. For every combination of SDD1 and SDD2 hits, the track vertex z was calculated using the z -position of the detectors and the r -coordinate of the two hits. The reconstructed z vertex was then shifted to the event coordinate system resulting in a

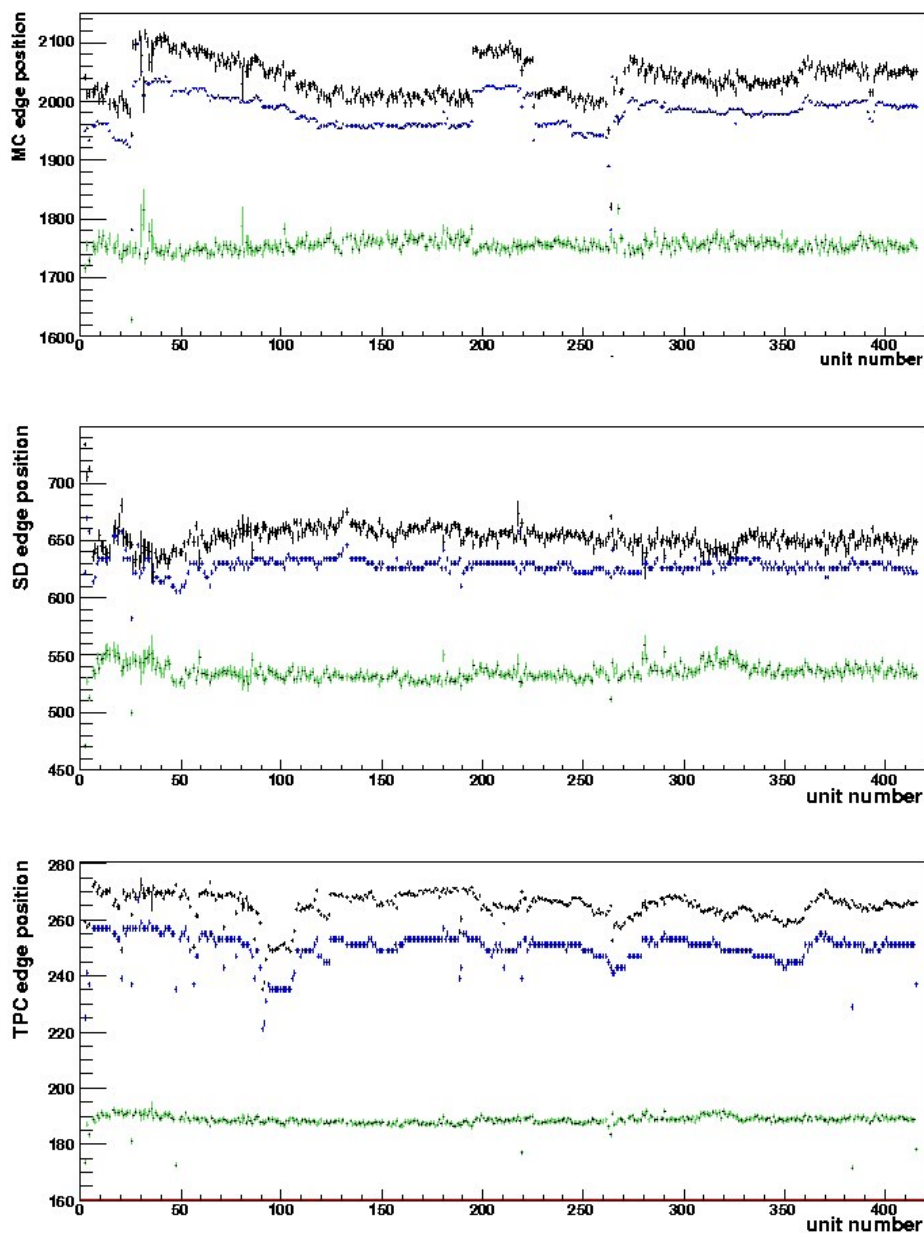


Figure 4.20: The edge position of multiplicity distributions as a function of the unit number determined via integration (blue) and via fit (black). The green plot shows the (arbitrarily scaled up) ratio of the two methods.

narrow peak positioned on a broad background of the random hit combination (see Fig. 4.22). The background subtraction procedure was based on the determination of z vertex position by

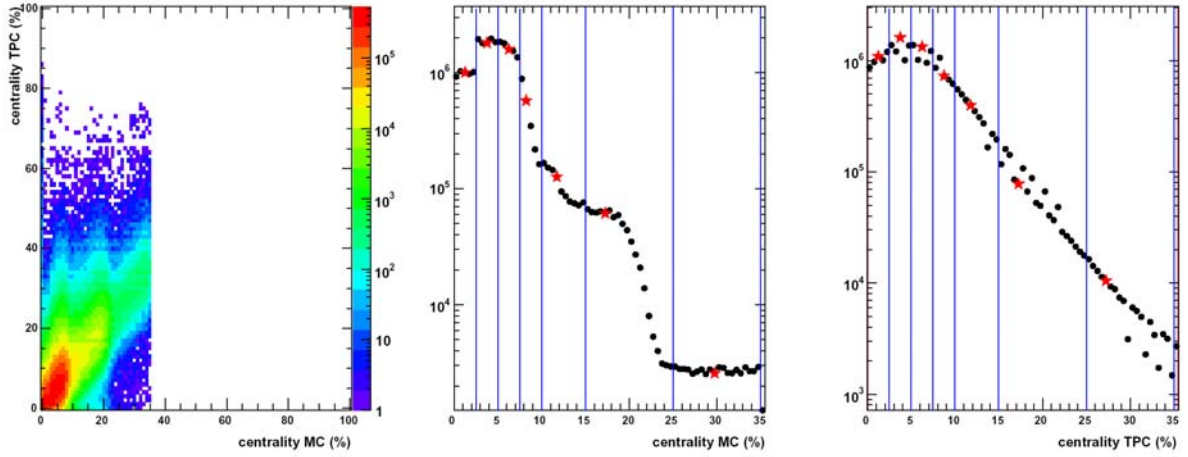


Figure 4.21: The calibrated centrality in percent of the geometrical cross section accumulated over all data set. Left panel: correlation between TPC and MC. Middle panel: centrality distribution recorded by MC. Right panel: centrality distribution recorded by the TPC. The solid lines represent the centrality selection used for the two particle correlation analysis presented in this thesis.

combining hits belonging to different ϕ regions e.g. $-1.81 < \phi < -1.61$ with $0.38 < \phi < 0.62$. The remaining peak was integrated from -1.2 cm to 1.2 cm, yielding the fake-free number of tracks originating from the vertex. This number was divided by the number of events and the ϕ -acceptance factor $\Delta\phi/(2 \cdot \pi) = 0.4/(2 \cdot \pi) = 0.0637$. Such procedure was performed separately in five bins of η covering $2 < \eta < 3$. The obtained $dN_{ch}/d\eta$ still has to be corrected

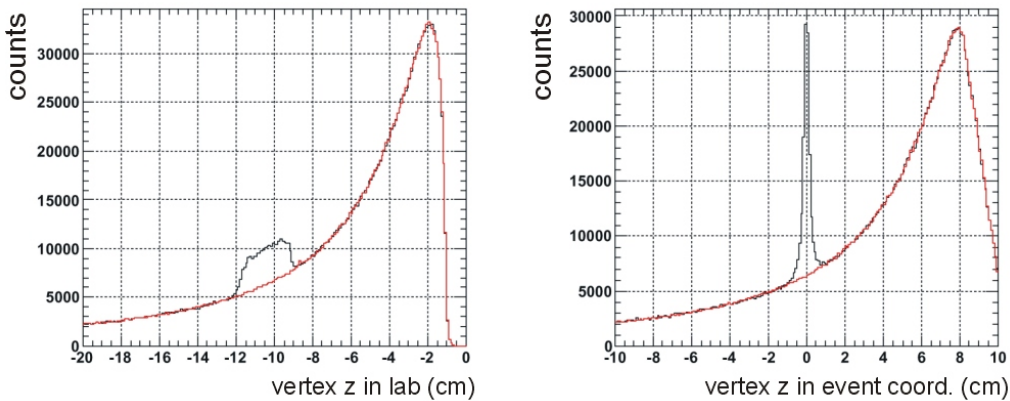


Figure 4.22: Vertex z distribution for the hit pairs from SDD1 and SDD2 in laboratory coordinate system (left) and in the event coordinates (right). The background distribution is depicted as a red line.

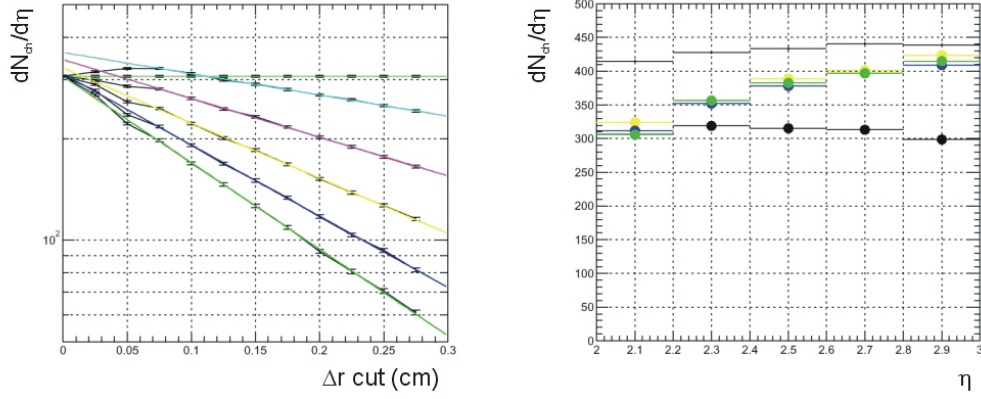


Figure 4.23: Left panel: an example of the extrapolation method for the η between 2.0 to 2.2. Right panel: the charged particle multiplicity as a function of the pseudorapidity for the event centrality integrated from 0 to 5 % of σ_{GEOM} . The raw data is depicted as a black points, the color points correspond to the values extrapolated at $\Delta r = 0$. For comparison, the results of a naive counting SDD tracks are shown as the black dots.

for the two-hit resolution and the δ -electrons coming from the target. The two-hit resolution is responsible for decreasing efficiency for the reconstruction of close tracks. In order to account for this effect, the procedure, described above, was repeated for different values of the two-hit separation cuts Δr and $\Delta\phi$. For a fixed $\Delta\phi$, $dN_{ch}/d\eta$ vs. Δr was fitted by an exponential function in the range $0.07 \text{ cm} < \Delta r < 0.21 \text{ cm}$ and extrapolated to zero (see Fig. 4.23). The extrapolated $dN_{ch}/d\eta(0)$, obtained in this fashion for $\Delta\phi=0.027$, 0.036 , and 0.045 are very similar. For the final result the histograms obtained with $\Delta\phi=0.036$ were used. The δ -electrons were estimated by applying the complete procedure for the beam trigger data (100 bursts of run 1423). The result was 16 electrons on average into the η -interval from 2 to 3. Half of this was then subtracted from the minimum bias run results to account for electrons knocked out of the targets preceding the one in which the interaction occurred.

The resulting $dN/d\eta$ values for different classes of centrality, corrected for the δ -electrons, are listed in Table 4.2. In addition, dN_{ch}/dy was calculated as $1.025 \times dN_{ch}/d\eta$, based on the UrQMD calculations. This result fits the available beam energy systematic (see Fig. 4.24).

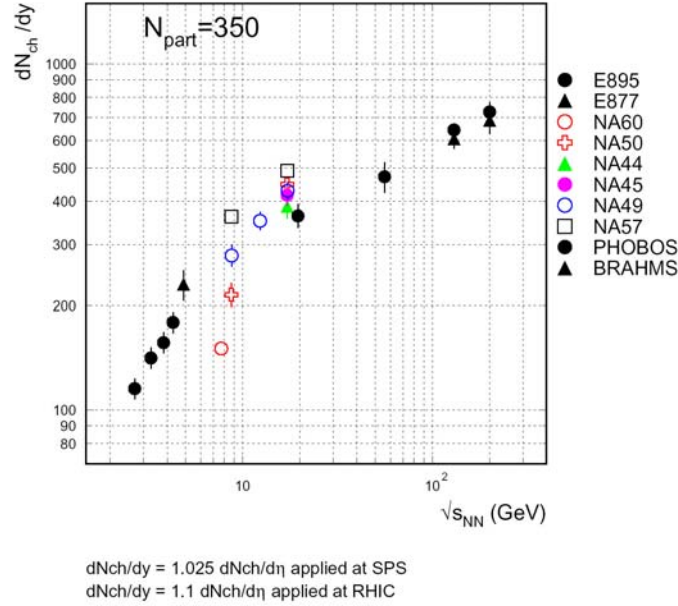


Figure 4.24: Beam energy dependence of the rapidity density of charge particle.

centrality (%)	$dN_{ch}/d\eta(3.1)$	$dN_{ch}/d\eta(2-3)$	$dN_{ch}/d\eta(2.1-2.65)$	$dN_{ch}/dy(2.91)$
0-5	404.4+-4.4	359.3+-2.4	347.2+-2.4	412.5+-4.5
5-10	340.1+-3.8	300.7+-2.1	291.6+-2.1	346.9+-3.9
10-15	278.7+-3.3	253.8+-1.8	246.1+-1.8	284.3+-3.3
15-20	230.5+-2.8	213.6+-1.6	209.0+-1.6	235.1+-2.8
20-25	189.9+-2.4	177.7+-1.4	173.7+-1.4	193.7+-2.5
25-30	157.8+-2.1	145.9+-1.2	144.2+-1.2	161.0+-2.2
30-35	132.2+-1.9	120.5+-1.1	117.7+-1.1	134.9+-1.9
35-40	107.6+-1.7	97.5+-1.0	94.2+-1.0	109.8+-1.8
40-45	89.5+-1.5	78.1+-0.9	75.6+-0.9	91.3+-1.5
45-50	69.9+-1.4	61.2+-0.8	58.8+-0.8	71.3+-1.4
50-55	54.4+-1.2	47.9+-0.7	46.2+-0.7	55.5+-1.2
55-60	43.9+-1.1	38.6+-0.6	37.5+-0.6	44.8+-1.1
60-65	35.2+-1.0	31.0+-0.6	29.9+-0.6	36.0+-1.0
65-70	30.0+-0.9	24.6+-0.5	22.6+-0.5	30.6+-1.0
70-75	23.7+-0.9	18.9+-0.5	17.2+-0.5	24.1+-0.9
75-80	16.1+-0.8	13.0+-0.4	12.0+-0.4	16.4+-0.8
80-85	11.1+-0.8	6.3+-0.4	5.2+-0.4	11.3+-0.8
85-90	329.2+-1215.9	0.4+-0.3	-0.1+-0.3	335.8+-1240.2

Table 4.2: The charged particle multiplicity $N_{ch}/d\eta$ and the rapidity density of charge particles extrapolated at the midrapidity for different centralities.